

# 1 Evolving viscous anisotropy in the upper mantle 2 and its geodynamic implications

3 Á. Király<sup>1</sup>, C.P. Conrad<sup>1</sup>, L.N. Hansen<sup>2</sup>

4 <sup>1</sup> Centre for Earth Evolution and Dynamics, University of Oslo, Norway

5 <sup>2</sup> Department of Earth and Environmental Sciences, University of Minnesota, Minneapolis,  
6 MN, USA

7

## 8 ***Key Points***

- 9 • We develop models of olivine texture evolution within deforming asthenosphere, and  
10 the associated directional variations in viscosity
- 11 • The effective viscosity of textured olivine can vary by an order of magnitude,  
12 depending on which slip system dominates the deformation.
- 13 • Anisotropic viscosity promotes faster plate motion & ridge-parallel subduction  
14 initiation, but impedes directional changes in plate motion

15

## 16 ***Key words***

17 Olivine, Anisotropic viscosity, LPO, Texture development, Plate motions, Asthenospheric  
18 deformation

19

20 ***Abstract***

21 Asthenospheric shear causes some minerals, particularly olivine, to develop anisotropic  
22 textures that can be detected seismically. In laboratory experiments, these textures are also  
23 associated with anisotropic viscous behavior, which should be important for geodynamic  
24 processes. To examine the role of anisotropic viscosity for asthenospheric deformation, we  
25 developed a numerical model of coupled anisotropic texture development and anisotropic  
26 viscosity, both calibrated with laboratory measurements of olivine aggregates. This model  
27 characterizes the time-dependent coupling between large-scale formation of lattice-preferred  
28 orientation (i.e., texture) and changes in asthenospheric viscosity for a series of simple  
29 deformation paths that represent upper-mantle geodynamic processes. We find that texture  
30 development beneath a moving surface plate tends to align the a-axes of olivine into the plate-  
31 motion direction, which weakens the effective viscosity in this direction and increases plate  
32 velocity for a given driving force. Our models indicate that the effective viscosity increases  
33 for shear in the horizontal direction perpendicular to the a-axes. This increase should slow  
34 plate motions and new texture development in this perpendicular direction, and could impede  
35 changes to the plate motion direction for 10s of Myrs. However, the same well-developed  
36 asthenospheric texture may foster subduction initiation perpendicular to the plate motion and  
37 deformations related to transform faults, as shearing on vertical planes seems to be favored  
38 across a sub-lithospheric olivine texture. These end-member cases examining shear-  
39 deformation in the presence of a well-formed asthenospheric texture illustrate the importance  
40 of the mean olivine orientation, and its associated viscous anisotropy, for a variety of  
41 geodynamic processes.

42

43 *Plain language summary*

44 The uppermost layer of Earth's mantle, the asthenosphere, experiences large deformations due  
45 to a variety of tectonic processes. During deformation, grains of olivine, the main rock-  
46 forming mineral in the asthenosphere, rotate into a preferred direction parallel to the  
47 deformation, developing a texture that can affect the response of the asthenosphere to tectonic  
48 stresses. Laboratory measurements show that the deformation rate depends on the orientation  
49 of the shear stress relative to the olivine texture. We use numerical models to apply the  
50 findings of the laboratory measurements to geodynamic situations that are difficult to simulate  
51 in a laboratory. These models track the development of olivine texture and its directional  
52 response to shear stress, which are highly coupled. Our results suggest that anisotropic  
53 viscosity in the asthenosphere can significantly affect the motions of tectonic plates, as plate  
54 motion in a continuous direction should become faster while abrupt changes in the direction  
55 of plate motion should meet high resistance in the underlying asthenosphere. We suggest that  
56 olivine textures in the asthenosphere play a critical role in upper mantle dynamics.

57

## 1. Introduction

59 The physical characteristics of the upper mantle, e.g. its density and rheology, control a  
60 variety of surface features, such as general tectonic regime, faulting characteristics, dynamic  
61 topography, and plate velocity. Many of these features are thus related to the properties of  
62 olivine, which comprises ~60% of the upper mantle (Stixrude and Lithgow-Bertelloni, 2005).  
63 It has long been known that olivine is anisotropic in its elastic properties, and this directional  
64 dependence has been observed in the upper mantle using seismic waves (e.g., Tanimoto and  
65 Anderson, 1984). This observed seismic anisotropy is mainly the result of the lattice preferred  
66 orientation (LPO, or texture) of the olivine crystals, which causes the speed of seismic waves  
67 to depend on propagation direction and additionally causes shear waves to split into two  
68 perpendicularly polarized waves (faster and slower) (Bamford and Crampin, 1977;  
69 Christensen, 1984; Mainprice et al., 2015). The texture (or LPO) itself is thought to result  
70 from shear strain in the upper mantle, which causes olivine crystals to rotate into a preferred  
71 direction, generally with the seismically fast axis parallel to the direction of shearing (e.g.,  
72 Ribe, 1989; Karato and Wu, 1993). Seismic observations of this anisotropy have been used to  
73 infer patterns of upper-mantle deformation (Long and Becker, 2010), for example related to  
74 tectonic plate motions (e.g., Becker, 2008; Becker et al., 2014, 2008, 2003; Behn et al., 2004;  
75 Conrad and Behn, 2010; Gaboret et al., 2003), subduction (e.g., Long, 2013), continental  
76 collision (e.g., Silver, 1996), and motion on transform faults (e.g., Eakin et al., 2018).

77 Early laboratory experiments found that olivine is not limited to anisotropy in its elastic  
78 properties, but also exhibits anisotropy in its viscosity. Durham and Goetze (1977)  
79 demonstrated that the deformation rate of a single olivine crystal is orientation dependent and  
80 can vary by a factor of 50. To assess the role of single-crystal anisotropy in controlling the  
81 anisotropy of an aggregate of crystals, Hansen et al. (2012) first deformed aggregates of  
82 olivine in torsion and subsequently deformed them in extension. In torsion, the samples  
83 gradually weaken as the texture forms, but subsequent extensional deformation normal to the  
84 initial shear plane is characterized by a factor of 14 increase in viscosity. Similarly, but in a  
85 reverse order, Hansen et al., (2016b) first deformed aggregates of olivine in extension and  
86 subsequently deformed them in torsion. In extension, the samples gradually weaken as the  
87 texture forms, but subsequent torsional deformation is again characterized by much higher  
88 viscosities. Taken together, these experiments demonstrate that prolonged deformation in a  
89 consistent orientation leads to texture formation that reduces the viscosity, and a subsequent  
90 change in the orientation of deformation results in a dramatic increase in the viscosity.

91 However, Hansen et al.'s (2016b) laboratory experiments were only able to test a small  
92 number of deformation paths (i.e., first extension, then torsion, and *vice versa*), making it  
93 difficult to directly apply their results to deformation in the mantle. To apply their results  
94 more generally to mantle deformation, Hansen et al., (2016a) used the existing experiments to  
95 define and calibrate a mechanical model of slip-system activities and texture development  
96 within olivine aggregates. This model can predict both the evolution of olivine textures and  
97 the associated anisotropic viscous behavior for olivine aggregates undergoing arbitrary  
98 deformation paths. This coupled micromechanical and textural development model enables us  
99 to investigate the role of viscous anisotropy for a range of geodynamic processes.

100 Decades ago, researchers used early numerical modeling techniques to test the relevance of  
101 viscous anisotropy on geodynamical processes, such as mantle convection or post-glacial  
102 rebound (Christensen, 1987). These studies relied on the laboratory measurements of Durham  
103 and Goetze (1977), which constrained the anisotropic behavior of single olivine crystals, and  
104 the work of Karato (1987), who studied the mechanisms of olivine texture formation. Due to  
105 the absence of more detailed laboratory data, previous modelers assumed transverse isotropy  
106 in a two-dimensional mantle (i.e., isotropic viscosity for shearing in the horizontal plane, and  
107 anisotropy expressed as differences between shearing in the horizontal and vertical  
108 directions). More recently, the effect of anisotropic viscosity on mantle convection has been  
109 revisited (Mühlhaus et al., 2003), with additional investigations into Raleigh-Taylor  
110 instabilities and subduction-zone processes within an anisotropically viscous mantle and/or  
111 lithosphere (Lev and Hager, 2011, 2008). These studies are based on the director method  
112 (Mühlhaus et al., 2002), which models olivine orientations as a set of directors, that is, 2D  
113 unit vectors pointing normal to the easy shear plane. Anisotropic viscosity is expressed by a  
114 combination of normal and shear viscosities, and the effective shear viscosity is a function of  
115 the distribution of the directors. Furthermore, because the directors are advected and rotated  
116 by the flow, this method effectively couples texture development to the anisotropic viscosity  
117 of the mantle. The 2D nature of the director method, however, limits its ability to capture the  
118 complete anisotropy associated with olivine, which has three independent slip systems that  
119 accommodate deformation at different rates (Hansen et al., 2016a).

120 Here we have modified the director method to accommodate three-dimensional deformations  
121 of olivine aggregates using the micromechanical approach of Hansen et al. (2016a). This  
122 model is calibrated by laboratory constraints on slip system activities and parameters of  
123 texture development (i.e., the relative rotation rates of the different olivine slip systems, see

124 Table 1 in Hansen et al, 2016a). The resulting model allows us to explore both the texture  
125 development of an olivine aggregate in a wide range of deformation paths and the mechanical  
126 response of these textured aggregates to applied stresses associated with these deformation  
127 paths. Our goal is to create first-order models of tectonic plate movement subject to a  
128 continuous driving force (e.g., slab pull) in one direction. As the olivine texture develops in  
129 the asthenosphere, we expect the mechanical response of the system to change as a function  
130 of time and accumulated strain, resulting in a changing plate velocity. Next, by changing the  
131 direction of the driving force, we can examine the response of the system to the application of  
132 stress in a new direction. The resulting deformation paths are analogs for geodynamic  
133 applications such as changes in the direction of plate movement, lithospheric dripping,  
134 initiation of subduction, and transform faulting. These simple exercises lead us to a better  
135 understanding of the interplay among olivine-texture development, anisotropic mantle  
136 rheology, and large-scale geodynamic processes.

## 137 **2. Methods**

### 138 **2.1 Mathematical formulation**

139 Our method is based on the micromechanical model described and characterized by Hansen et  
140 al. (2016a). This approach uses a pseudo-Taylor approximation (after Taylor, 1938) to  
141 calculate the stress needed to create an equivalent strain rate on each olivine crystal, allowing  
142 for slip along three linearly independent slip systems. Each slip system is characterized by a  
143 critical shear stress that describes its strength relative to the isotropic strength of the  
144 aggregate. The best-fit model parameters obtained by Hansen et al. (2016a) for the pseudo-  
145 Taylor model are the following: 0.30 for the (010)[100] slip system, 0.27 for the (001)[100]  
146 slip system, and 1.29 for the (010)[001] slip system. The micromechanical model is coupled  
147 to a texture development model, in which the deformation of the olivine aggregate results in  
148 grain rotations. The rotation rate depends on the orientation of each grain with respect to the  
149 deformation, and a set of texture parameters that define the relative rotation rates along the  
150 four olivine slip systems (see Table 1 in Hansen et al., 2016a). These combined models  
151 provide the basis for a method to calculate the anisotropic viscosity (or conversely, the  
152 fluidity) for any given olivine texture. The resulting three-dimensional tensor can then be used  
153 to predict the deformation behavior for several geodynamic applications. In the following, we  
154 present details of this method and the results of first-order models in which the olivine-rich

155 upper mantle undergoes different deformation paths induced by temporal variations in an  
 156 applied shear stress.

157 To calculate the strain rate induced by the imposed stress, some further steps are necessary  
 158 beyond those described by the mechanical model of Hansen et al. (2016a). The macroscopic  
 159 constitutive relationship between stress and strain rate for an anisotropic viscous medium is

$$160 \quad \sigma_{kl} = \eta_{ijkl} \dot{\epsilon}_{ij}, \quad (1)$$

161 where  $\dot{\epsilon}_{ij} = \frac{1}{2} \left( \frac{\partial v_i}{\partial x_j} + \frac{\partial v_j}{\partial x_i} \right)$  is the strain-rate tensor,  $\sigma_{kl}$  is the deviatoric-stress tensor, and  $\eta_{ijkl}$   
 162 is the viscosity tensor (Christensen, 1987; Pouilloux et al., 2007). Due to their symmetry, the  
 163 deviatoric-stress and the strain-rate tensors can both be reduced to vectors using Kelvin  
 164 notation, which preserves the norm of each of the tensors in (1) (Dellinger et al., 1998),

$$165 \quad \dot{\epsilon}_{ij} = \begin{bmatrix} \dot{\epsilon}_{11} & \dot{\epsilon}_{12} & \dot{\epsilon}_{13} \\ \dot{\epsilon}_{12} & \dot{\epsilon}_{22} & \dot{\epsilon}_{23} \\ \dot{\epsilon}_{13} & \dot{\epsilon}_{23} & \dot{\epsilon}_{33} \end{bmatrix} \equiv \begin{bmatrix} \dot{\epsilon}_{11} \\ \dot{\epsilon}_{22} \\ \dot{\epsilon}_{33} \\ \sqrt{2}\dot{\epsilon}_{23} \\ \sqrt{2}\dot{\epsilon}_{13} \\ \sqrt{2}\dot{\epsilon}_{12} \end{bmatrix} \equiv \begin{bmatrix} \dot{\epsilon}_1 \\ \dot{\epsilon}_2 \\ \dot{\epsilon}_3 \\ \dot{\epsilon}_4 \\ \dot{\epsilon}_5 \\ \dot{\epsilon}_6 \end{bmatrix} \quad (2)$$

166

$$167 \quad \sigma_{ij} = \begin{bmatrix} \sigma_{11} & \sigma_{12} & \sigma_{13} \\ \sigma_{12} & \sigma_{22} & \sigma_{23} \\ \sigma_{13} & \sigma_{23} & \sigma_{33} \end{bmatrix} \equiv \begin{bmatrix} \sigma_{11} \\ \sigma_{22} \\ \sigma_{33} \\ \sqrt{2}\sigma_{23} \\ \sqrt{2}\sigma_{13} \\ \sqrt{2}\sigma_{12} \end{bmatrix} \equiv \begin{bmatrix} \sigma_1 \\ \sigma_2 \\ \sigma_3 \\ \sigma_4 \\ \sigma_5 \\ \sigma_6 \end{bmatrix}. \quad (3)$$

168 It follows that the viscosity can be reduced to a 6x6 tensor (e.g., Pouilloux et al., 2007).  
 169 Because of the non-linear rheological behavior of olivine, the viscosity tensor is also a  
 170 function of stress. The rheology can thus be expressed by a stress-independent material  
 171 constant ( $\underline{A}$ ), which relates to the viscosity as

$$172 \quad \text{inv}(\eta_{ij}) = A_{ij} \cdot II_{\sigma}^{(n-1)/2}. \quad (4)$$

173 Equation 4 describes the fluidity of the material at a given stress, where  $II_{\sigma}$  denotes the  
 174 second invariant of the deviatoric stress and  $n$  is the power-law factor. Using eq. (4), the strain  
 175 rate can be expressed as a function of the stress and the fluidity according to

$$176 \quad \begin{bmatrix} \dot{\varepsilon}_1 \\ \dot{\varepsilon}_2 \\ \dot{\varepsilon}_3 \\ \dot{\varepsilon}_4 \\ \dot{\varepsilon}_5 \\ \dot{\varepsilon}_6 \end{bmatrix} = \begin{bmatrix} A_{11} & A_{12} & A_{13} & A_{14} & A_{15} & A_{16} \\ A_{21} & A_{22} & A_{23} & A_{24} & A_{25} & A_{26} \\ A_{31} & A_{32} & A_{33} & A_{34} & A_{35} & A_{36} \\ A_{41} & A_{42} & A_{43} & A_{44} & A_{45} & A_{46} \\ A_{51} & A_{52} & A_{53} & A_{54} & A_{55} & A_{56} \\ A_{61} & A_{62} & A_{63} & A_{64} & A_{65} & A_{66} \end{bmatrix} \cdot \begin{bmatrix} \sigma_1 \\ \sigma_2 \\ \sigma_3 \\ \sigma_4 \\ \sigma_5 \\ \sigma_6 \end{bmatrix} \cdot II_{\sigma}^{(n-1)/2}. \quad (5)$$

177 To solve eq. (5) for the strain rate, the material constant  $\underline{\underline{A}}$ , which we will refer to as the  
 178 fluidity parameter tensor, must be known.  $\underline{\underline{A}}$  is a function of temperature and grain size, but  
 179 also depends on the crystal orientations of the aggregate. The micromechanical model of  
 180 Hansen et al. (2016a) allows us to find the stress needed to produce any strain rate for a given  
 181 olivine texture. Therefore, to find the components of  $\underline{\underline{A}}$  with the pseudo-Taylor mechanical  
 182 model, we need to apply 6 different strain rates to the aggregate and calculate the 6 stress  
 183 vectors that are required to produce these strain rates. The six strain rates define the columns  
 184 of the tensor  $\underline{\underline{E}}$

$$185 \quad E = \begin{bmatrix} \dot{\varepsilon}_0 & -\dot{\varepsilon}_0/2 & -\dot{\varepsilon}_0/2 & 0 & 0 & 0 \\ -\dot{\varepsilon}_0/2 & \dot{\varepsilon}_0 & -\dot{\varepsilon}_0/2 & 0 & 0 & 0 \\ -\dot{\varepsilon}_0/2 & -\dot{\varepsilon}_0/2 & \dot{\varepsilon}_0 & 0 & 0 & 0 \\ 0 & 0 & 0 & \dot{\varepsilon}_0/\sqrt{2} & 0 & 0 \\ 0 & 0 & 0 & 0 & \dot{\varepsilon}_0/\sqrt{2} & 0 \\ 0 & 0 & 0 & 0 & 0 & \dot{\varepsilon}_0/\sqrt{2} \end{bmatrix}, \quad (6)$$

186 where  $\dot{\varepsilon}_0$  is the applied strain rate amplitude. By applying the micromechanical model of  
 187 Hansen et al. (2016a) separately to each column of  $\underline{\underline{E}}$ , we can compute the set of stress tensors  
 188 associated with each of these six strain rates. We use these stress tensors to construct the  
 189 tensor  $\underline{\underline{S}}$ , for which each row represents the stress vector associated with the strain-rate vector  
 190 in each column of  $\underline{\underline{E}}$ , multiplied by  $II_{\sigma}^{(n-1)/2}$ . These two tensors are related according to the  
 191 equation

$$192 \quad \underline{\underline{E}} = \underline{\underline{A}} \cdot \underline{\underline{S}}, \quad (7)$$

193 where  $\underline{\underline{S}} =$

$$\begin{bmatrix} II_{\sigma_1}^{(n-1)/2} \sigma_{1_1} & II_{\sigma_1}^{(n-1)/2} \sigma_{2_1} & II_{\sigma_1}^{(n-1)/2} \sigma_{3_1} & II_{\sigma_1}^{(n-1)/2} \sigma_{4_1} & II_{\sigma_1}^{(n-1)/2} \sigma_{5_1} & II_{\sigma_1}^{(n-1)/2} \sigma_{6_1} \\ II_{\sigma_2}^{(n-1)/2} \sigma_{1_2} & II_{\sigma_2}^{(n-1)/2} \sigma_{2_2} & II_{\sigma_2}^{(n-1)/2} \sigma_{3_2} & II_{\sigma_2}^{(n-1)/2} \sigma_{4_3} & II_{\sigma_2}^{(n-1)/2} \sigma_{5_2} & II_{\sigma_2}^{(n-1)/2} \sigma_{2_2} \\ II_{\sigma_3}^{(n-1)/2} \sigma_{1_3} & II_{\sigma_3}^{(n-1)/2} \sigma_{2_3} & II_{\sigma_3}^{(n-1)/2} \sigma_{3_3} & II_{\sigma_3}^{(n-1)/2} \sigma_{4_3} & II_{\sigma_3}^{(n-1)/2} \sigma_{5_3} & II_{\sigma_3}^{(n-1)/2} \sigma_{6_3} \\ II_{\sigma_4}^{(n-1)/2} \sigma_{1_4} & II_{\sigma_4}^{(n-1)/2} \sigma_{2_4} & II_{\sigma_4}^{(n-1)/2} \sigma_{3_4} & II_{\sigma_4}^{(n-1)/2} \sigma_{4_4} & II_{\sigma_4}^{(n-1)/2} \sigma_{5_4} & II_{\sigma_4}^{(n-1)/2} \sigma_{6_4} \\ II_{\sigma_5}^{(n-1)/2} \sigma_{1_5} & II_{\sigma_5}^{(n-1)/2} \sigma_{2_5} & II_{\sigma_5}^{(n-1)/2} \sigma_{3_5} & II_{\sigma_5}^{(n-1)/2} \sigma_{4_5} & II_{\sigma_5}^{(n-1)/2} \sigma_{5_5} & II_{\sigma_5}^{(n-1)/2} \sigma_{6_5} \\ II_{\sigma_6}^{(n-1)/2} \sigma_{1_6} & II_{\sigma_6}^{(n-1)/2} \sigma_{2_6} & II_{\sigma_6}^{(n-1)/2} \sigma_{3_6} & II_{\sigma_6}^{(n-1)/2} \sigma_{4_6} & II_{\sigma_6}^{(n-1)/2} \sigma_{5_6} & II_{\sigma_6}^{(n-1)/2} \sigma_{6_6} \end{bmatrix}$$

194 In  $\underline{\underline{S}}$ ,  $\sigma_{ij}$  denotes the  $i^{\text{th}}$  component of the deviatoric stress in Kelvin notation corresponding to  
 195 the  $j^{\text{th}}$  column of  $\underline{\underline{E}}$ , calculated with the pseudo-Taylor method described by (Hansen et al.,  
 196 2016a), and  $II_{\sigma_j}$  is the second invariant of each stress tensor (corresponding to the  $j^{\text{th}}$  column  
 197 of  $\underline{\underline{E}}$ ). Equation (7) needs to be inverted to determine  $\underline{\underline{A}}$ . However, due to the  
 198 incompressibility criteria and because  $\underline{\underline{S}}$  builds up by deviatoric stresses,  $\sum_{i=1}^3 E_{ij} = 0 \wedge$   
 199  $\sum_{i=1}^3 S_{ij} = 0$  for each  $j$ . This means that  $\underline{\underline{S}}$  is not invertible in its full form. However, we do  
 200 not lose information by reducing both  $\underline{\underline{E}}$  and  $\underline{\underline{S}}$  by one column and one row (the first column  
 201 and row) because the first component of both the strain rate and the deviatoric stress can be  
 202 reconstructed from their second and third components. This reduction yields  $\underline{\underline{E}}' = \underline{\underline{A}}' \cdot \underline{\underline{S}}'$ , where  
 203 each matrix has 5 rows and columns and a rank of 5. Hence,  $\underline{\underline{S}}'$  is invertible, so

$$204 \quad \underline{\underline{A}}' = \underline{\underline{E}}' \cdot \underline{\underline{S}}'^{-1} \quad (8)$$

205 can be solved.

206 Knowing the fluidity parameter tensor,  $\underline{\underline{A}}'_*$  for a given olivine texture allows us to compute  
 207 the full strain-rate tensor for any given applied stress tensor. The actual deformation that is  
 208 produced depends on model assumptions about how this deformation is geodynamically  
 209 expressed in the rock. In this study, we examine geodynamic processes associated with simple  
 210 shear of the asthenosphere, e.g., as produced by the motion of a surface plate over an  
 211 asthenospheric layer (Figure 1). To implement this deformation, we impose a deformation  
 212 gradient consistent with simple shear, for which the deformation tensor ( $D_{ij} = \partial u_i / \partial x_j$ ) is

$$213 \quad D_{F_1} = \begin{bmatrix} 0 & 2\dot{\epsilon}_{12} & 2\dot{\epsilon}_{13} \\ 0 & 0 & 2\dot{\epsilon}_{23} \\ 0 & 0 & 0 \end{bmatrix} \quad (9)$$

214 for the case in which the asthenosphere is sheared with force  $F_1$  (Fig. 1) and thus driven by a  
 215 stress  $\sigma_{13}$ . The deformation that results is described in (9) by  $D_{12}$ ,  $D_{23}$ , and  $D_{13}$ , where  $D_{12}$  and  
 216  $D_{23}$  are only excited because of the anisotropic nature of the rheology. Note that we neglect  
 217 the normal strain rate components ( $D_{11}=D_{22}=D_{33}=0$ ) assuming that the geometric constraints  
 218 on the system do not permit net elongation or contraction in any direction. From the imposed  
 219 deformation, we can calculate the associated texture evolution as a function of time for a  
 220 given applied stress history. The time-step in the calculation is set based on the strain rate to  
 221 have 0.1 strain increment for each time-step, which we have found to produce stable results.

## 222           2.2 Geodynamic model

223 To investigate the influence of anisotropic viscous behavior in geodynamic scenarios with  
224 changing orientations of stress, we model the deformation of a set of olivine grains  
225 representing the behavior of the asthenosphere. We apply a shear stress (=force/area) of 0.68  
226 MPa, which roughly corresponds to the shear stress acting on a plate of area 6000 km by 6000  
227 km that is necessary to balance an edge force of  $4.1 \cdot 10^{12}$  N/m (a lower bound estimate for  
228 the value of slab pull force transferred to the plate from the negative buoyancy of a  
229 subducting oceanic lithosphere; Schellart, 2004) above a 200-km-thick asthenosphere (*Fig.*  
230 *1A*). We track the deformation of the asthenosphere using the micromechanical model of  
231 texture-development and viscous anisotropy described above. Based on the anisotropic  
232 properties of a representative olivine aggregate, we compute the strain rate within the  
233 asthenosphere, and associated parameters such as plate speed and movement direction, all as a  
234 function of time, accumulated strain, and olivine texture development. To calculate the plate  
235 velocity, we assume that the velocity is 0 at the base of the  $H_a = 200$  km thick asthenosphere  
236 and that the horizontal velocity at the top of the asthenosphere is the plate velocity, hence

$$237 \quad V_{plate} = 2 \cdot \sqrt{\dot{\epsilon}_{13}^2 + \dot{\epsilon}_{23}^2} \cdot H_a \quad (10)$$

238 To investigate different deformation paths that are analogs for a variety of upper mantle  
239 processes, we change the orientation of the applied shear stress, and consequently the  
240 deformation applied to the asthenosphere, at a chosen instant after an olivine texture has  
241 formed (*Fig. 1B*). Such a change could be induced by a change in the external driving forces  
242 applied to the asthenosphere. An intuitively simple approach would be to rotate the imposed  
243 driving stress relative to the texture that initially formed. However, for numerical and  
244 analytical simplicity, we instead rotate the olivine texture with respect to the imposed stress  
245 (as shown in *Fig. 1C*), which is held steady. This approach produces an equivalent result and  
246 allows us to keep the definition of both the shear stress and the deformation tensors (equation  
247 9) unchanged. Later, we will discuss the geodynamic scenarios represented by the various  
248 rotations of the olive texture with respect to the applied shear stress.

249 We define the angles  $\alpha$  and  $\beta$  as the orientations of the imposed shear stress and the resulting  
250 plate motion with respect to a coordinate system fixed in the asthenosphere (x-axis, *Fig. 1C*).  
251 Thus,  $\alpha$  is the angle between the (1)-axis (which is the same as the direction of the shear  
252 stress) and the x-axis (which is the angle of rotation of the texture) in *Fig. 1*, and  $\beta$  is the angle

253 between the plate motion direction and the (x)-axis. The horizontal shear components of the  
254 strain rate ( $\dot{\epsilon}_{23} \wedge \dot{\epsilon}_{13}$ ) are used to calculate the direction of the plate movement ( $\beta$ ), as follows:

$$255 \quad \beta = \text{atan}\left(\frac{\dot{\epsilon}_{23}}{\dot{\epsilon}_{13}}\right) + \alpha \quad (9)$$

### 256 **3. Results**

257 We present the results of 27 models with different deformation paths. Each model result is an  
258 average of 5 individual runs, each initiated with 1000 olivine grains with initial orientations  
259 randomly drawn from a uniform distribution. Therefore, we effectively represent the  
260 asthenosphere under a large (6000x6000 km<sup>2</sup>) plate using the average of 5 model runs of 1000  
261 grains each.

#### 262 **3.1. Monotonic simple shear**

263 First, we present the evolution of asthenospheric strain rates and olivine texture development  
264 from a uniformly distributed texture (i.e., an isotropic mantle) to a well-developed texture  
265 (anisotropic, weak mantle). As the mantle accumulates strain, the a-axes of olivine rotate  
266 towards the shear direction (*Fig. 1B*), developing a texture that decreases the effective  
267 viscosity of the asthenosphere and, therefore, increases the velocity of the plate. We examined  
268 two sets of models differing only in the randomly created uniformly distributed orientations at  
269 the start of the models (*Fig. 2*, black and grey curves). The similarity of these two model  
270 averages implies that the average of model runs with 5x1000 grains gives a reasonably stable  
271 result. However, subtle differences in the initial textures of the two models can still cause  
272 minor differences in the amplitudes of the fluidity parameters (*Fig. 2B*).

273 The amplitude of the shear strain rate ( $|\dot{\epsilon}| = 2 \cdot \sqrt{\dot{\epsilon}_{12}^2 + \dot{\epsilon}_{13}^2 + \dot{\epsilon}_{23}^2}$ , simply referred to as  
274 strain rate hereafter) exhibits characteristic variations throughout this deformation (*Fig. 2*),  
275 which result from the texture evolution of the olivine aggregates and the associated changes in  
276 the fluidity parameter tensor (*Fig. 2B and 2C*). With an initially uniform olivine distribution,  
277 the strain rate in the asthenosphere is  $1.5\text{-}1.7 \cdot 10^{-14} \text{ s}^{-1}$ , which corresponds to a plate velocity of  
278  $\sim 9.5\text{-}10.5 \text{ cm/yr}$  velocity. As accumulated strain increases, the olivine texture develops, the  
279 effective viscosity of the asthenosphere decreases, and the plate velocity increases, reaching a  
280 maximum of  $14.8 \text{ cm/yr}$  ( $2.4 \cdot 10^{-14} \text{ s}^{-1}$ ) around a strain of 8, i.e. after  $\sim 14 \text{ Myr}$  of shearing.  
281 With further shearing, the plate velocity decreases and subsequently stabilizes at  $12.3 \text{ cm/yr}$   
282 ( $1.9 \cdot 10^{-14} \text{ 1/s}$ ). The effective viscosity is inversely proportional to the strain rate, reaching a  
283 minimum at  $\sim 14.5 \text{ Myr}$  (strain of 8) and slightly increasing during the later history. The

284 magnitude of the viscosity varies from  $2.9\text{-}4.5 \times 10^{19}$  Pa·s. Hence, with continuous shearing,  
285 any further evolution of the olivine texture decreases the asthenosphere's effective viscosity  
286 by less than a factor of 2.

287 Both the shear components of the fluidity tensor ( $A_{44}$ ,  $A_{55}$ ,  $A_{66}$  in *Fig. 2B*) and the off-diagonal  
288 components ( $A_{45}$  and  $A_{65}$  in *Fig. 2C*) exhibit variations with time as the olivine texture  
289 develops. The non-zero component of the stress tensor is  $\sigma_{13}$ , ( $\sigma_5$  in Kelvin notation), which  
290 means that  $A_{55}$  represents the fluidity in the shear direction (shearing on the (3) plane in the  
291 (1) direction, creating  $\partial v_1/\partial x_3$ ). Note that since  $\sigma_{31} = \sigma_{13}$  (symmetry of the stress tensor),  
292 then  $A_{55}$  also represents the fluidity for the reciprocal deformation (i.e., shearing on the (1)  
293 plane in the (3) direction, creating  $\partial v_3/\partial x_1$ ).  $A_{44}$  and  $A_{66}$  represent the values of the fluidity  
294 that would control the deformation (shearing given by  $\partial v_3/\partial x_2$  or  $\partial v_2/\partial x_3$  for  $A_{44}$  and by  
295  $\partial v_1/\partial x_2$  or  $\partial v_2/\partial x_1$  for  $A_{66}$ ) if we were to change the shear stress to  $\sigma_{23}$  ( $=\sigma_{32}$ ) or  $\sigma_{12}$   
296 ( $=\sigma_{21}$ ), respectively.

297 Initially, there is no preferred orientation of the olivine grains, and the three shear fluidity  
298 components are the same. As the asthenosphere deforms and the texture develops in  
299 association with shearing on the (3) plane in the (1) direction,  $A_{55}$  increases, which is  
300 associated with a decrease in viscosity and an increase in the plate velocity. In contrast, the  
301 fluidity component  $A_{44}$  ( $A_{2323}$ ) decreases, which indicates that it would become harder and  
302 harder to shear the asthenosphere with a stress  $\sigma_{23}$ , which would induce shearing on the (3)  
303 plane in the (2) direction (i.e., plate motion in a perpendicular direction), or reciprocally on  
304 the (2) plane in the (3) direction. Surprisingly,  $A_{66}$  increases with progressive deformation,  
305 and most of the time is even larger than  $A_{55}$ . Thus, as the texture develops, it also becomes  
306 easier to shear the asthenosphere along the vertical (2) plane in the (3) direction (or,  
307 reciprocally, along the (3) plane in the (2) direction). The  $A_{45}$  and  $A_{65}$  off-diagonal  
308 components (*Fig. 2C*) are noteworthy because these components couple  $\sigma_{13}$  to  $\dot{\epsilon}_{23}$  and  $\dot{\epsilon}_{12}$ ,  
309 respectively (eq. 5). These components are initially zero, but do take on finite values with  
310 progressive deformation. In other words, as the anisotropy of the system develops, the applied  
311 shear stress begins to induce shear strains on planes other than the primary shear plane, and in  
312 directions other than the primary shear direction. However, because these components are two  
313 orders of magnitude lower than  $A_{55}$ , the strain rate in this simple case is dominated by the  
314 effects of  $A_{55}$ . Consequently, values of  $A_{55}$  (*Fig. 2B*), strain rate (*Fig. 2D&E*), and plate  
315 velocity (*Fig. 2D*) all exhibit the same trend as a function of time and strain.

316

### 317 3.1.1. Rheology and texture parameters

318 As demonstrated above, the plate velocity (calculated from the horizontal strain rate) and the  
319 shear-parallel ( $A_{55}$ ) component of the fluidity tensor are linearly dependent, and those terms  
320 are inversely proportional to the effective viscosity. To further understand the initially  
321 increasing and subsequently decreasing evolution of the strain rate, the relationship between  
322 the texture and the rheological behavior of the asthenosphere (olivine aggregate) needs to be  
323 examined. In the literature, a number of texture parameters have been proposed to quantify  
324 the orientation distribution of a group of crystals. For example, the J-index (also referred to as  
325 the texture strength) provides a metric for the degree of alignment of crystal orientations  
326 (Bunge, 1982), varying between 1 (uniform distribution) and infinity (single-crystal texture).  
327 The M-index (Skemer et al., 2005) also assesses the degree of alignment and results from the  
328 difference between the uncorrelated and the uniform misorientation-angle distributions, with a  
329 value between 0 (uniform distribution) and 1 (single-crystal texture). We calculated both the  
330 J- and the M- indices with MTEX (Mainprice et al., 2015) and plotted the latter along with the  
331 plate velocity against the accumulated strain (*Fig. 3A*). Comparing the two curves (blue and  
332 yellow, for the plate velocity and the M-index, respectively), no direct relationship is  
333 observable.

334 We examine the subtleties of the textural development with pole-figures that indicate the  
335 orientation distributions of the three main axes of the olivine grains (*Fig.3*). These plots  
336 illustrate that better correlation may be found between the plate velocity and the distributions  
337 of individual axes instead of the M-index, which describes the orientation distribution of all  
338 three axes. For example, as the plate velocity decreases between the strains of 8 and 16, the  
339 distributions of the a- and c-axes become more girdled, while the distribution of the b-axes  
340 becomes more clustered, resulting in an increasing M-index. Thus, the qualitative comparison  
341 of the pole figures with the plate velocity suggests that the distribution of a-axes, which  
342 represents the easiest slip direction, exerts a primary influence on the rheological behavior of  
343 the aggregate.

344 Therefore, we calculate three additional parameters that describe the degree to which the  
345 orientation distribution is random ( $R$ ), girdle-like ( $G$ ) or point-like ( $P$ ), for each  
346 crystallographic axis (a-axes:  $P-a$ ,  $G-a$ ,  $R-a$ ; b-axes:  $P-b$ ,  $G-b$ ,  $R-b$ ; c-axes  $P-c$ ,  $G-c$ ,  $R-c$ )  
347 (Vollmer, 1990). All three parameters vary between 0 and 1, and the sum of all three  
348 parameters is 1 for each axis distribution. We plot these texture parameters against the  
349 accumulated strain and the plate velocity (*Fig. 3A*), revealing some correlation between the  $P$ -

350  $a$  values and the plate velocity and some anticorrelation between the  $G$ - $a$  values and the plate  
351 velocity.

352

### 353 **3.2. Change in the direction of the shear force**

354 The aim of this section is to test several deformation paths that, to first order, represent those  
355 expected for different geodynamic processes. For example, changing the force acting on the  
356 plate from the (1) direction to the (2) direction (i.e., from force  $F_1$  to force  $F_2$  in *Fig. 4*)  
357 represents a change in the direction of the pull force acting on a tectonic plate, and should  
358 change the direction of plate movement (*Fig. 4*). Other changes to the force that we explore  
359 are illustrated in *Fig. 4*. These force directions can mimic shearing induced by subduction  
360 initiation and/or drizzling ( $F_3$  and  $F_5$ ) or the start of transform faulting ( $F_4$  and  $F_6$ ).

361 First, we describe the results of an instantaneous change in the direction of the asthenospheric  
362 shear force (from  $F_1$  to  $F_2$ ,  $F_3$ ,  $F_4$ ,  $F_5$ , or  $F_6$  in *Fig. 4*). We then examine the influence on the  
363 deformation behavior of (1) the rate of rotation of the shear force direction (from 1 Myr/90° to  
364 12 Myr/90°), (2) the amount of texture development prior to the change, and (3) the total  
365 rotation angle of the driving stress when switching from  $F_1$  to  $F_2$ . As noted above, we  
366 implement a change in the driving force (or shear stress) by rotating the textured olivine  
367 aggregate (formed by applying the shear of model 1 for a chosen amount of accumulated  
368 strain) while keeping the shear stress constant (*Fig. 1C*).

#### 369 3.2.1 Instantaneous change in shear direction

370 At a strain of 8 (i.e., after shearing the olivine aggregate for 14.5 Myr), the  $a$ -axes distribution  
371 reaches the maximum value of  $P$  (*Fig. 3*). Hence, to maximize the effect of anisotropy in our  
372 tests, we first reach a shear strain of 8 by applying  $\sigma_{13}$  with deformation consistent with  
373 applying the force  $F_1$  (using the same initial texture as in model 1), then switching to a new  
374 force direction (defined in *Fig. 4*). Due to the symmetric nature of the stress tensor,  $F_3$  is  
375 achieved using the same applied stress as  $F_1$ , but by employing different applied boundary  
376 conditions that enforce deformation consistent with vertical shearing, i.e.:  $D_{F_3} =$

377  $\begin{bmatrix} 0 & 0 & 0 \\ 2\dot{\epsilon}_{12} & 0 & 0 \\ 2\dot{\epsilon}_{13} & 2\dot{\epsilon}_{23} & 0 \end{bmatrix} = D_{F_1}^T \cdot F_2$  and  $F_5$  are consistent with a stress tensor in which only  $\sigma_{23}$  and

378  $\sigma_{32}$  are non-zero and deformation is given by  $D_{F_2} = \begin{bmatrix} 0 & 0 & 2\dot{\epsilon}_{13} \\ 2\dot{\epsilon}_{12} & 0 & 2\dot{\epsilon}_{23} \\ 0 & 0 & 0 \end{bmatrix} \wedge D_{F_5} = D_{F_2}^T \cdot F_4$  and

379  $F_6$  are both consistent with a stress tensor where only  $\sigma_{12}$  and  $\sigma_{21}$  are non-zero and induce

380 deformation given by  $D_{F_4} = \begin{bmatrix} 0 & 2\dot{\epsilon}_{12} & 2\dot{\epsilon}_{13} \\ 0 & 0 & 0 \\ 0 & 2\dot{\epsilon}_{23} & 0 \end{bmatrix} \wedge D_{F_6} = D_{F_4}^T$ . As mentioned before, these

381 deformations are equivalent to those achieved by rotating the mantle (i.e. the olivine  
382 aggregate) with respect to the force  $F_1$  and keeping the imposed boundary conditions  
383 expressed by the deformation tensor  $D_{F_1}$  (equation 9). A  $90^\circ$  rotation of the aggregate around  
384 the  $x$ -axis represents a change from  $F_1$  to  $F_4$ , around the  $y$ -axis reproduces  $F_3$ , and around the  
385  $z$ -axis reproduces  $F_2$ .  $F_5$  is modeled by rotating the aggregate around the  $x$ - and then  $z$ -axes,  
386 and  $F_6$  is modeled by rotation around the  $x$ - then  $y$ -axes. Referring to *Fig. 4*, rotating the  
387 aggregate around its  $x$  or its  $x$  then  $y$  axes represents shearing produced by a transform fault  
388 ( $F_4$  or  $F_6$ ), rotation around the  $y$  or the  $x$  then  $z$  axes represents shearing associated with  
389 dripping or subduction ( $F_3$  or  $F_5$ ), while rotation around the  $z$  axis represents a change in the  
390 direction of the horizontal shear ( $F_2$ ) (e.g., due to a change in the direction of slab pull force).

391 The effect of changing the shear direction largely depends on the direction of the new shear  
392 stress with respect to the textured mantle (*Fig. 5*). For example, when the rotation results in a  
393 new shear stress that primarily induces deformation on the hardest (010)[001] slip system ( $F_2$   
394 or  $F_5$ ), the strain rate decreases dramatically, from  $2.3 \cdot 10^{-14}$  to  $4.9 \cdot 10^{-15} \text{ s}^{-1}$  (*Fig. 5B*, orange  
395 and green curves). Translating to plate velocity, this change implies a decrease from 14.8  
396 cm/yr to 3 cm/yr.

397 Note that reciprocal pairs of shear deformations (that is,  $F_1$ - $F_3$ ,  $F_2$ - $F_5$ , and  $F_4$ - $F_6$ ) are  
398 associated with the same stress state (shear stress given by  $\sigma_{13}$ ,  $\sigma_{23}$ ,  $\sigma_{12}$ , respectively) and  
399 initially activate the same slip systems because they are deforming the same initial texture.  
400 Thus, the effective viscosity, and the associated deformation rates, for each of these pairs is  
401 initially the same (as shown at a strain of 8 in *Figs. 5A, 5B, and 5C*, respectively). However,  
402 because the rotation associated with these deformation pairs is different (because we employ  
403 different boundary conditions  $D$ ), the textures for these pairs evolve differently (*Fig. 5*, right  
404 column), and their strain-rates diverge (*Fig. 5*, left column).

#### 405 3.2.1.1 Representing change in plate motion direction

406 Rotating the olivine aggregate around its  $z$ -axis represents a relative change in the direction of  
407 the plate driving force. The result of a model with  $90^\circ$  instantaneous rotation (green curve in  
408 *Fig. 5B*) exhibits a dramatic reduction in strain rate and a slow recovery of the olivine texture  
409 after the rotation. By the end of the model run (total shear strain of 21) the strain rate has

410 increased to  $1.3 \cdot 10^{-14} \text{ s}^{-1}$ , which is still less than the strain rate for the initially isotropic  
411 aggregate. Because of the slow deformation associated with the diminished strain rate, this  
412 partial recovery took almost 50 Myr. Examination of the change in olivine texture directly  
413 after the rotation (at strain of 8.5, *Fig. 5*) illustrates that the orientations are well organized but  
414 that the preferred orientation is perpendicular to the direction of shearing (*Fig. 5*). When the  
415 strain rate finally starts to increase, the a-axis distribution is more random or girdle-like rather  
416 than point-like, even at a total strain of 21. Regarding the fluidity tensor, when the texture is  
417 rotated, the  $A_{55}$  component (which relates  $\sigma_{13}$  to  $\dot{\epsilon}_{13}$ ) decreases while both  $A_{45}$  and  $A_{65}$  exhibit  
418 a minor increase, leading to similar values for all three components.

### 419 *3.2.1.2 Shear forces associated with transform faults*

420 There are two possibilities for creating shear stress in a horizontal direction along a vertical  
421 plane, which roughly approximates the stress state associated with a transform fault. The  
422 possible shear forces are  $F_4$  or  $F_6$  (*Fig. 4*), which produce very different paths in the strain-rate  
423 evolution (*Fig. 5C*) if there is already a well-developed texture associated with deformation  
424 due to  $F_1$ . At the time of rotation (at a strain of 8), both models exhibit an elevated strain rate  
425 (to  $3.3 \cdot 10^{-14} \text{ s}^{-1}$ ) compared to the earlier deformation (driven by  $F_1$ ). The pink curve,  
426 representing the switch from  $F_1$  to  $F_4$ , after the initial peak strain rate, slowly decreases to  
427  $\sim 1.5 \cdot 10^{-14} \text{ s}^{-1}$ . Switching from  $F_1$  to  $F_6$  is relatively easy, as the model exhibits increasing  
428 strain rate (up to  $\sim 6.7 \cdot 10^{-14} \text{ s}^{-1}$ ) associated with the texture evolution after the rotation for an  
429 additional shear strain of  $\sim 4$  (*Fig. 5C*, dark blue curve). This peak is followed by a quickly  
430 decreasing strain rate that stabilizes around  $\sim 2 \cdot 10^{-14} \text{ s}^{-1}$ , which is comparable to the strain rate  
431 for larger strains in reference model 1 (black curve). The high strain rate produced by the  
432 model representing  $F_6$  is associated with a quick texture evolution and a point-like  
433 distribution in the new shear direction that is more strongly aligned than the distribution prior  
434 to the change in shear direction. In contrast, changing from  $F_1$  to  $F_4$  (rotation around the  $x$ -  
435 axes) keeps the a-axis distribution basically aligned with the shear direction, but with  
436 subsequent strain, the a-axis distribution forms a girdle, decreasing the initial point-like  
437 distribution and leading to slower strain rates than prior to the change in shear direction.

### 438 *3.2.1.3 Shear forces associated with dripping/subduction*

439 There are two possibilities for creating shear stress in a vertical direction as a rough  
440 approximation of the stress state associated with subduction or dripping instabilities.  
441 Changing from  $F_1$  to  $F_3$  (texture rotation around the  $y$ -axis; *Fig. 4*), results in initial

442 deformation occurring at the same rate as for  $F_1$  (because  $F_1$  and  $F_3$  are reciprocal  
443 deformations, as described above) followed by a decrease in strain rate (i.e. small increase in  
444 the effective viscosity) as the texture evolves (*Fig. 5A*, cyan curve). Subsequent texture  
445 evolution produces a period with increasing strain rate, between strains of 8.5 (0.5 after the  
446 switch) to 13, peaking at  $4.4 \cdot 10^{-14} \text{ s}^{-1}$ . The model results exhibit a decreasing trend in strain  
447 rate immediately after this peak, reaching a final strain rate of  $2 \cdot 10^{-14} \text{ s}^{-1}$  (after a total strain of  
448 21). In contrast, changing from  $F_1$  to  $F_5$  (orange curve in *Fig. 5B*) induces a dramatically  
449 diminished strain rate ( $5 \cdot 10^{-15} \text{ s}^{-1}$ , equivalent to that produced by  $F_2$  as described above) that  
450 slowly recovers over the next 20-25 Myr (by a total strain of 14) and stabilizes around 2.2-  
451  $2.3 \cdot 10^{-14} \text{ s}^{-1}$ , which is slightly higher than the strain rate at high stresses in model 1. Similar to  
452 the “transform fault” models, the strain-rate curves for “subduction/dripping” can be linked to  
453 the texture development. The higher strain rate at the end of the model that applies  $F_5$  (x- then  
454 y- rotation) compared to the model end after applying  $F_3$  results from a more point-like  
455 distribution of the olivine a-axes (*Fig. 5A&B*).

### 456 3.2.2. Rate of rotation of the stress orientation

457 In the preceding section, the change in texture orientation relative to the applied forces was  
458 instantaneous. In the following sections, the rate, timing, and amount of rotation of the olivine  
459 aggregate are examined. Here we focus on the simplest case, a change in the plate-motion  
460 direction ( $F_1$  changing to  $F_2$ ). Here, we impose a  $90^\circ$  rotation over a time interval ranging  
461 from 1 to 13 Myr, after  $\sim 14$  Myr of initial shearing (an accumulated strain of 8).

462 As described above, we use  $\alpha$  and  $\beta$  (eq. 9) to indicate the angle between the x-axis (in the  
463 aggregate reference frame) and the shear force and plate motion directions, respectively.  
464 During rotation of the aggregate,  $\alpha$  linearly changes with time from  $0^\circ$  to  $-90^\circ$ . In contrast, the  
465 angle  $\beta$  does not change linearly with time and can differ from  $\alpha$  significantly because the  
466 olivine texture excites plate motion differently in varied directions. During the rotation period,  
467 and independently of its duration, the plate movement differs from the shear direction by up  
468 to  $20^\circ$  (*Fig. 6A*). Minor differences can be observed depending on the rotation rate. Once  $90^\circ$   
469 rotation is achieved, the plate movement is either parallel to the shear direction (1 and 10 Myr  
470 rotation period), overturned (3 and 5 Myr rotation period) or rotated less than the shear  
471 direction (13 Myr rotation period). After rotation, all models evolve in a similar manner,  
472 resulting in velocity vectors  $15\text{-}20^\circ$  away from the shear direction. The plate speed drastically  
473 decreases, reaching 3 cm/yr by the end of the rotation period (*Fig. 6B*). As in the  
474 instantaneous rotation model, the plate movement cannot recover its original rate after the

475 rotation (*Fig. 6B*). The models with shorter rotation time (1-5 Myr) reach a maximum of 7  
476 cm/yr while the models with longer texture rotation time (10-13 Myr) reach a maximum of 5  
477 cm/yr by the end of the model (at strain  $\sim 20$ -21). Interestingly, during the first  $\sim 4^\circ$  of  
478 rotation, the plate velocity increases, except for the model with 1 Myr rotation time, where the  
479 rotation step is  $9^\circ/\text{timestep}$  (as the timestep is fixed to 100 kyr during the rotation). This  
480 increase can be explained by the mean orientation of the olivine texture (see pole figures for a  
481 strain of 8 on *Fig. 3*) and the plate movement (*Fig. 6A*) before the onset of rotation, which are  
482 both a few degrees ( $\sim 4^\circ$  and  $-1.2^\circ$ , resp.) offset from the shear direction. Hence, at the onset  
483 of rotation, the texture initially becomes more aligned with the shearing, resulting in up to 2  
484 cm/yr increase in the plate velocity (see texture evolution animations, which are available in  
485 the supplementary materials for each model).

### 486 3.2.3. Role of texture evolution prior to the rotation

487 In an additional series of calculations, we varied the amount of accumulated strain between 2  
488 and 14 prior to a  $90^\circ$  rotation, which was implemented using two different rotation rates ( $90^\circ$   
489 and  $9^\circ/\text{Myr}$ ).

490 The magnitude of the velocity decrease associated with rotation appears to be proportional to  
491 the textural maturity of the aggregate before rotation (*Fig. 7B*). However, the rate of rotation  
492 has only a small effect, as described previously (*Fig. 6*). Note that for the models in which the  
493 rotation is imposed after a strain of 11 or 14, faster rotation results in a slightly lower  
494 minimum plate velocity (*Fig. 7D*). Only the model with fast and early rotation (rotation at a  
495 strain of 2) exhibits velocities that return to the original plate velocity magnitude, while the  
496 other models reach strain of 21 with only 5.4-8.4 cm/yr plate velocity (*Fig. 7B*).

497 A large range of variation in the plate motion direction can be observed depending on the  
498 amount of initial strain, rotation rate, and time/total accumulated strain (*Fig. 7A & C*). In most  
499 of the models, the difference  $\alpha$ - $\beta$  grows from  $\sim -1^\circ$  to  $\sim 15$ - $20^\circ$  during rotation (see the two  
500 outlined circles in each line on *Fig. 7C*), which is also the maximum difference between  $\alpha$  and  
501  $\beta$ . There are three slight outlier models, in which extreme magnitudes of  $\alpha$ - $\beta$  occur during the  
502 model evolution. With an initial strain of 5 and a slow-rotation rate, the plate motion direction  
503 can differ from the shear direction by up to  $29^\circ$ , while in the models in which an initial strain  
504 of 14 is imposed, the plate-motion direction rotates more than the shear direction, reaching  
505 extremes of  $-6^\circ$  and  $-21^\circ$  (with 1 and 10 Myr rotation time, respectively).

506

## 3.2.4. Role of the amount of rotation

507 In more realistic geodynamic scenarios, the driving forces on plates are unlikely to rotate as  
508 much as  $90^\circ$ , so we additionally tested a range of rotations from  $22^\circ$  to  $90^\circ$  degrees with slow  
509 ( $9^\circ/\text{Myr}$ ) and fast ( $90^\circ/\text{Myr}$ ) rotation rates. In all of these models, the aggregate was sheared  
510 with force  $F_I$  until a strain of 8 prior to the rotation. We found (*Fig. 8*) that the larger the  
511 rotation, the lower the average strain rate, and therefore the lower the average plate velocity  
512 (*Fig. 8B&D*). Furthermore, the models with faster rotation rates exhibit a greater variability of  
513 plate motion directions and velocities than the models with slower rotation rates (*Fig. 8*).  
514 With only  $22^\circ$  rotation,  $\beta$  differs from  $\alpha$  by only  $15^\circ$  during the rotation in both models, and  
515 this difference linearly decreases as the model progresses until, at the end of the model, the  
516 plate motion becomes parallel to the shear direction. The plate velocity decreases to 7.5-7.8  
517 cm/yr, which then climbs back to the isotropic rate ( $\sim 10$  cm/yr) by the end of the models. If  
518 the total change in shear direction is  $45^\circ$  or more, all models result in  $\sim 20^\circ$  difference between  
519  $\alpha$  and  $\beta$  during the rotation, independent of the rate of rotation. Later, the models with slower  
520 rotation rate result in even larger differences between  $\alpha$  and  $\beta$ . The plate motion direction can  
521 change more quickly if the plate velocity is high, such as in the model with  $45^\circ$  rotation at  
522  $90^\circ/\text{Myr}$  during the period between 25 and 35 Myr (*Fig. 8B*). On the other hand, in the model  
523 with  $67^\circ$  rotation at  $9^\circ/\text{Myr}$ , the plate velocity remains between 3.5-5 cm/yr, and  $\alpha$ - $\beta$  remains  
524  $\sim 20^\circ$  (15-25°).

525

**4. Discussion**

526 The results described above suggest that the effective viscosity and strain rate of the  
527 asthenosphere, and the associated plate velocity at the surface, are extremely sensitive to the  
528 olivine texture. The asthenosphere weakens as the olivine texture develops with the a-axes  
529 parallel to the shear direction ('anisotropic weak' on *Fig. 1B*), allowing for a 40% increase in  
530 plate velocity (or equally, decrease in effective viscosity). The asthenosphere acts 'strong'  
531 (*Fig. 1C*) if the mean a-axes direction is perpendicular to, and the mean c-axes direction is  
532 parallel to, the shear direction. In this case, the effective viscosity is up to  $\sim 5$  times higher  
533 than if the a-axes are parallel to the shear force, resulting in a slower plate velocity that is only  
534 a third of the velocity over the isotropic asthenosphere and a fifth of that in the 'anisotropic  
535 weak' case (*Fig. 10*). This difference in viscosity is in accordance with the differences in the  
536 strengths of the slip systems (Table 1 in Hansen et al., 2016a), favoring deformation parallel  
537 to the a-axes (i.e. on the (010)[100] and (001)[100] slip systems, with strengths of 0.3 and

538 0.27, respectively) versus parallel to the c-axes (where the strength of the (010)[001] slip  
539 system is 1.29). Thus, deformations that dominantly activate the (010)[100] slip system (e.g.,  
540  $F_1$  and  $F_3$  at a strain of 8, *Fig. 5A*) and the (001)[100] slip system (e.g.,  $F_4$  and  $F_6$  at a strain of  
541 8, *Fig. 5C*) exhibit much faster strain rates compared to those that dominantly activate the  
542 (010)[001] slip system (e.g.,  $F_2$  and  $F_5$  at a strain of 8, *Fig. 5B*).

543 The evolution of the plate velocity and plate-motion direction (or the entire matrix of  $\dot{\epsilon}$ ) is a  
544 function of the olivine texture, which evolves due to the deformation. Hence the  
545 asthenospheric rheology depends on the kinematics and vice-versa. Indeed, the models with  
546 an instantaneous change in the force direction demonstrate that applying the same stress but  
547 with different velocity boundary conditions (i.e. enforcing deformations consistent with  
548 individual forces on the asthenosphere, as shown on *Fig. 4*) can produce very different strain  
549 rate histories (e.g. *Fig. 5*, right column). For example, after creating a texture by force  $F_1$ ,  
550 switching to  $F_2$  or  $F_5$  both involve the same new stress state and both initially activate the  
551 same (010)[001] slip system. Thus, both deformations initially produce the same (although  
552 much reduced) strain rate (*Fig. 5B*). However, enforcing shear deformation in the vertical  
553 direction (i.e. by  $F_5$ ) allows for faster rotations of the olivine grains into the new shear  
554 direction, allowing for higher strain rates as the texture develops.

555 Without changes in the shear force direction, the plate-velocity evolution follows a similar  
556 trend to the values of  $P$ -a (point-like distribution value for the olivine a-axes) (*Fig. 3*).  
557 However, if the direction of the shear force changes, this correlation is less clear. We  
558 calculated the texture parameters described in section 3.1.1 for each model for a 0.5 strain  
559 increment, for which an example is presented in *Figure 9*. If the texture is rotated  $90^\circ$  around  
560 the z-axis with respect to the shear stress (in 1 Myr), then the changes in the values of  $P$ -a are  
561 no longer correlated to the changes in the plate velocity, especially around the time of the  
562 rotation (between a strain of 8 and 11), at which point the values of  $P$  for the a-, b-, and c-axes  
563 ( $P$ -a,  $P$ -b,  $P$ -c) and the M-index are the largest (*Fig. 9*), while the plate velocity is the lowest.

564 To analyze the overall relationship between texture parameters and kinematic parameters (e.g.  
565 plate velocity), we performed a Pearce correlation for all the models representing shearing by  
566 plate pull. The correlation values between the plate velocity and texture parameters (*Fig. 9*)  
567 demonstrate that the mean orientation of the olivine a-axes (*ori-a* on *Fig. 9*) as well as the  
568 mean orientation of the c-axes (*ori-c*) are highly anticorrelated with the plate velocity. In  
569 contrast,  $P$ -a has the highest correlation with the plate velocity of 0.64, which is similar to the  
570 strength of the anticorrelation between the G-value (girdle-like distribution) of the a-axes (G-

571 *a*) and the plate velocity ( $v_{plate}$ ). It is important to note that these parameters are not  
572 independent from each other, as *G-a* and *P-a* are anticorrelated with a coefficient of -0.94  
573 (similarly, -0.83 between *G-b* and *P-b*) and a 0.85 correlation between *ori-a* and *ori-c* (*Suppl.*  
574 *Fig. S1*). Based on the correlation between the texture parameters and the plate velocity, as  
575 well as between each pair of texture parameters, we find that the plate velocity can be linked  
576 essentially to two parameters, the mean orientation and the value of *P* for the distribution of  
577 the *a*-axes of the olivine grains, and therefore we see the strongest correlation between the  
578 plate velocity and the product of those two parameters ( $P-a \cdot \cos(ori-a)$  in *Figure 9*).

579 The need to consider both mean orientation and value of *P* for the *a*-axes provides important  
580 context for comparison to previous investigations of texture evolution in olivine. Boneh et al.  
581 (2015) used DRex, a different model of texture evolution (Kaminski and Ribe, 2002), to  
582 investigate the influence of changing the deformation kinematics on texture. By examining  
583 scenarios similar to our cases *F*<sub>2</sub> and *F*<sub>3</sub>, Boneh et al. (2015) concluded that olivine texture  
584 evolves to a new steady state by a shear strain of ~4. This conclusion was based on tracking  
585 the dominant *a*-axis orientation, and is consistent with our observations (*Fig. 5*). However,  
586 our investigation of the mechanical response of an olivine aggregate suggests that the  
587 evolution of the viscosity can be considerably more protracted (especially for *F*<sub>2</sub>), and our  
588 correlation analysis demonstrates that additional features of the texture, most notably *P-a*, are  
589 likely responsible for that difference.

590 The orientation of the olivine grains also exerts an important control on the direction of the  
591 plate motion (or asthenospheric flow) with respect to the driving force. As noted above, in the  
592 case of continuous shearing in one direction, the shear stress induces very little non-parallel  
593 shear strain, but as soon as the shear direction is changed toward the mean orientation of the  
594 olivine *c*-axes (i.e. the strongest slip system), we observe an increase in strain rates in  
595 directions that are non-parallel to the shear stress. While the relationship between these  
596 factors is not straightforward, it is clear that as *ori-a* starts to differ from the shear direction,  
597 there is a corresponding change in the plate-motion direction (*Fig. 7 & 8*). The highest values  
598 of  $\beta$  (plate-motion direction) occur at times in which *ori-a* differs 30-60° from the shear  
599 direction. When this angle is higher,  $\beta$  decreases to ~0°, and the plate velocity slows  
600 considerably. This behavior occurs because it is not possible to create strain perpendicular to  
601 the forcing. Thus, when a grain is oriented such that the *a*-axis is perpendicular to the shear  
602 direction, the easiest slip system cannot be activated (*Suppl. Fig. S2*).

603        **5. *Relevance to natural phenomena***

604        Although our models are simplistic by nature, we can use them to gain some intuition about  
605        how viscous anisotropy may affect different geodynamic processes. However, before we  
606        proceed, it is important to note the limitations of our models. In particular, we have assumed  
607        that the asthenosphere under a large (6000x6000 km<sup>2</sup>) plate deforms uniformly, and therefore  
608        the olivine texture, and its associated rheology, changes uniformly under the entire plate.  
609        Certainly, we may expect some textural heterogeneity for most realistic geodynamic  
610        scenarios, and this complexity may localize or otherwise change deformation patterns,  
611        affecting the results. Furthermore, our assumption that deformation occurs in a 200-km thick  
612        homogeneous layer of asthenosphere does not account for the possibility that deformation  
613        may be shifted to deeper layers if asthenospheric textures act to increase the asthenosphere's  
614        effective viscosity. Indeed, such a scenario is consistent with layered anisotropic textures  
615        under continents (e.g., Yuan and Romanowicz, 2010) and oceans (e.g., Beghein et al., 2014).  
616        Furthermore, other factors not included in our model, such as the presence of melt or strain  
617        localization, may affect deformation and/or textural development. As an example, our model  
618        also does not explicitly account for dynamic recrystallization, which Signorelli and Tommasi,  
619        (2015) showed can slightly increase the rate of fabric realignment relative to models with no  
620        recrystallization. However, our model parameters are calibrated based on laboratory  
621        experiments that inherently include such recrystallization (Hansen et al., 2016a, 2016b), and  
622        therefore, any application of this model assumes that rates of dynamic recrystallization are  
623        similar to those in laboratory experiments.

624        Despite these caveats, our simple experiments suggest that the textural anisotropy of the  
625        mantle should be associated with directional differences in effective viscosity that can be  
626        large (up to order of magnitude) and can change with time as textures develop. Anisotropic  
627        viscosity should thus influence a range of different geodynamic processes, and we can use our  
628        simple models to identify these influences (*Fig. 10*). In particular, depending on the  
629        orientation of the tectonic force with respect to the mean orientation of the olivine grains, and  
630        with respect to the three slip systems that can accommodate deformation, the anisotropic  
631        texture may either assist or resist continued deformation for a given process. This means that  
632        anisotropic viscosity may facilitate certain types of tectonic processes and impede others. We  
633        can thus use our simple models to generally characterize the expected trends relating viscous  
634        anisotropy to geodynamic processes. More quantitative characterization of the impact of  
635        viscous anisotropy will require more sophisticated modeling efforts.

## 5.1 Change in the direction of plate motion

637 By changing the orientation of the shear force in the horizontal direction (e.g. *Fig. 5A*), we  
638 demonstrate that the asthenospheric texture should significantly influence the motion of a  
639 tectonic plate. Indeed, for horizontally-oriented shear, the effective viscosity of an olivine  
640 aggregate may be a factor of ~5 times smaller when the shear force is parallel to the mean  
641 orientation of the a-axis of olivine grains (*ori-a*) compared to perpendicular to *ori-a* (*Fig. 10*).  
642 Thus, if the texture beneath the plate is characterized by strong alignment of the a-axes, then a  
643 large change in the orientation of forces on the plate may result in a significant slowing of the  
644 plate velocity (up to a factor of 5 in the case of a uniformly-deforming asthenosphere), even if  
645 the change in the orientation of forces occurs over a period of more than 10 million years  
646 (*Fig. 6*). The stronger the initial texture (e.g., formed as a result of strains greater than 2, *Fig.*  
647 *7*), and the larger the change in the orientation of the plate driving force (e.g., more than 45°,  
648 *Fig. 8*), the larger and more lasting the asthenospheric resistance will be to changes in the  
649 orientation of the driving forces. This asthenospheric resistance, induced by shear forces  
650 misaligned with the preferred orientation of the texture, can also result in plate motion that is  
651 not parallel to the plate driving force (*Figs. 6A, 7A, 8A*). This misalignment can last for 10s of  
652 millions of years because the asthenospheric texture may be slow to redevelop.

653 Thus, we expect that anisotropic viscosity may significantly modify the relationship between  
654 plate motions and the forces that drive them (e.g., Becker et al., 2006; Conrad and Lithgow-  
655 Bertelloni, 2004). Although Becker and Kawakatsu (2011) found that mantle flow models that  
656 included viscosity anisotropy behaved similarly to isotropic models, their study did not  
657 examine time-dependent behavior. Instead, our results suggest that time-dependent changes to  
658 the driving forces on plates, or to the amplitude or orientation of the anisotropic texture  
659 beneath them, should result in potentially large differences between the orientation of the net  
660 driving force on a plate and the direction of the resulting asthenospheric flow and plate  
661 motion. Note that the effective viscosity of the asthenosphere may also vary spatially beneath  
662 the plate depending on the orientation and maturity of the olivine texture locally. These  
663 spatial, temporal, and directional differences in the resistance that the asthenosphere exerts on  
664 plate motions may persist for durations of 10s of Myr (e.g., *Fig. 8*).

665 Our results suggest that anisotropic viscosity may cause a plate to respond only sluggishly to  
666 changes in the direction of its driving forces. Indeed, plate motions in global plate  
667 reconstruction models are observed to remain relatively stable for long periods (10s of Myr),  
668 except for a few brief periods of global reorganization (Bercovici et al., 2000). This overall

669 stability has been attributed to slow evolution of the plate driving forces (e.g., Richards and  
670 Lithgow-Bertelloni, 1996), despite the possibility that slab breakoff (Andrews and Billen,  
671 2009) or even a change in the direction and magnitude of subduction-related stresses (e.g.,  
672 Capitanio et al., 2011; Jahren et al., 2005) may change the driving forces on plates quickly.  
673 The sluggishness with which anisotropic textures adjust to changes in the orientation of the  
674 applied driving force may represent an alternative mechanism to explain the gradual changes  
675 in the direction of plate motions observed in reconstructions. This mechanism predicts that  
676 driving forces, asthenospheric resistance, and hence plate motions may be misaligned for  
677 significant periods of time. Indeed such misalignment might be relevant for the Pacific plate  
678 over the past 20 Myr (Faccenna et al., 2012).

## 679 **5.2 Transform faults**

680 Asthenospheric mantle, sheared by plate motions, should experience shear stresses in a  
681 horizontal direction on vertical planes near transform faults. Strain that results from these  
682 stresses will be enhanced by viscous anisotropy. If the shearing direction is parallel to the  
683 plate motions that generated the asthenospheric texture ( $F_4$  in *Fig. 4*; *Fig. 5C*; *Fig. 10*) the  
684 initially weakened asthenosphere will likely become stronger due to the evolving texture that  
685 results in a strengthening, girdle-like distribution. For transform motion perpendicular to this  
686 texture ( $F_6$  in *Fig. 4*; *Fig. 5C*; *Fig. 10*), the initial rotation of the olivine grains significantly  
687 weakens the asthenosphere. Interestingly, the results of this simple analysis are consistent  
688 with the large number of transform faults in the oceanic lithosphere. Although transform  
689 faults usually form close to the ridge where the asthenosphere has not been sheared for long,  
690 and where texture development involves a more complicated history associated with corner  
691 flow (Blackman et al., 2017), it is possible that the low asthenospheric resistance aids the  
692 formation of lithospheric scale transform faults.

## 693 **5.3 Initiation of subduction or dripping**

694 Changing the direction of the shear force from horizontal to vertical can be roughly associated  
695 with the initiation of slab subduction or dripping of lithospheric mantle. Our results ( $F_3$  and  $F_5$   
696 in *Fig. 5A&B*, *Fig. 10*) suggest that asthenosphere with well-oriented olivine grains imposes  
697 small resistance for such processes if they are oriented perpendicular to the initial plate-  
698 motion direction, but large resistance if they are oriented on the plane that is parallel to the  
699 plate motion. This finding is consistent with the observed orientation of subduction trenches,  
700 which are usually close to perpendicular to the long-term plate motion direction. Motion in

701 response to a vertically-oriented shear force on a plane perpendicular to the initial plate-  
702 motion direction (e.g, trench-perpendicular subduction,  $F_3$  in *Figure 4*) exhibits a short period  
703 of increased resistance to deformation that must be overcome before the texture weakens  
704 (*Figure 5C*, blue curve). Thus, asthenospheric textures may initially pose a slight impediment  
705 to subduction initiation, but after a few Myrs, the olivine texture evolution may hasten the  
706 evolution of subduction. In contrast, vertical motion in response to a vertical shear force on a  
707 plane parallel to plate motions (e.g., very oblique subduction or Richter-rolls,  $F_1$  to  $F_5$  in *Fig.*  
708 *4*) is highly resisted by the anisotropic fabric, but in the long term, olivine texture  
709 development induces asthenospheric weakening, which may allow for accelerated growth of  
710 lithospheric instabilities (*Fig. 5B*, orange curve).

711 However, both subduction initiation and small-scale convection involve more complex  
712 deformation than the simple instantaneous change in shear direction that is modeled here. For  
713 example, subduction zones often start along transform faults or in the vicinity of active  
714 subductions (Cramer et al., 2020), both of which can fundamentally change the  
715 asthenospheric texture and hence its resistance to the formation of new slabs or lithospheric  
716 instabilities. The rheology of the lithosphere also plays a potentially large role in subduction  
717 initiation, and it is possible that olivine texture can become frozen into the oceanic lithosphere  
718 as it cools (Tommasi, 1998), which would likely affect the rheology of the plate, and hence,  
719 its resistance to bending. Although analysis of this deformation is beyond the scope of this  
720 study, the combined effect of asthenospheric and lithospheric weakening due to anisotropy  
721 could allow for subduction zone initiation in response to lower tectonic stresses than usually  
722 expected (e.g., Gurnis et al., 2004). To explore the role of asthenospheric and lithospheric  
723 viscous anisotropy in such complex processes, more sophisticated 3D geodynamic modeling  
724 is required.

725

## 726 **6. Conclusions**

727 Olivine texture development in the asthenosphere and its response to shearing are highly  
728 coupled and can exert considerable influences on geodynamic processes. In response to  
729 unidirectional shearing of the asthenosphere, the formation of an olivine texture causes a  
730 significant decrease in effective mantle viscosity after accumulating a shear strain of  $\sim 5$ . After  
731 this texture has formed, changes to the direction of the forces on the system, as induced by a  
732 change in the tectonic setting, result in a different effective viscosity because of the

733 mechanically anisotropic nature of the textured asthenosphere. Our results indicate that  
734 differences in the effective viscosity associated with shearing asthenosphere primarily result  
735 from the relative activation of olivine's weak and strong slip systems. The resulting  
736 differences in effective viscosity can be over an order of magnitude, and should hinder some  
737 tectonic processes and foster others, depending on their sense of deformation relative to  
738 asthenospheric textures (*Fig. 10*). If the new shear direction is such that the strongest slip  
739 system, (010)[001], has to be activated to produce deformation, then the effective viscosity  
740 will increase. This increase is generally the case for a change in the direction of plate motion  
741 or vertical shearing on a plane parallel to plate motions. In contrast, the mantle should remain  
742 weak, or even become weaker, for shear forces that primarily induce deformation on the other  
743 two, weaker slip systems, (010)[100] and (001)[100], which is the case for transform motions,  
744 subduction initiation, or ongoing plate motion in the same direction. Thus, based on our  
745 simple models, we expect asthenospheric textures to significantly slow changes to the  
746 direction of plate motions and hinder the formation of ridge-perpendicular subduction zones.  
747 Conversely, these textures should assist in the initiation of new subduction zones parallel to  
748 mid-ocean ridges (perpendicular to plate motion) and promote the development of  
749 lithospheric scale transform faults. To fully understand the impact of anisotropic viscosity on  
750 plate tectonics and asthenospheric dynamics, olivine texture development, and the anisotropic  
751 viscosity that is associated with it, needs to be integrated into 3D dynamic models of the  
752 relevant processes.

## 753 **Acknowledgement**

754 This manuscript was significantly improved by constructive feedback from two anonymous  
755 reviewers. This work was supported by the Research Council of Norway Centres of  
756 Excellence project 223272. Data and code availability: <https://doi.org/10.11582/2020.00039>  
757 (Please also refer to the supplementary material for more information about the model data  
758 and code).

759

## 760 **References**

761 Andrews, E.R., Billen, M.I., 2009. Rheologic controls on the dynamics of slab detachment.  
762 Tectonophysics, Interpreting the tectonic evolution of Pacific Rim margins using plate

763 kinematics and slab window volcanism 464, 60–69.  
764 <https://doi.org/10.1016/j.tecto.2007.09.004>

765 Bamford, D., Crampin, S., 1977. Seismic anisotropy - the state of the art. *Geophysical Journal*  
766 *Of The Royal Astronomical Society* 49, 1–8. [https://doi.org/10.1111/j.1365-](https://doi.org/10.1111/j.1365-246X.1977.tb03697.x)  
767 [246X.1977.tb03697.x](https://doi.org/10.1111/j.1365-246X.1977.tb03697.x)

768 Becker, T.W., 2008. Azimuthal seismic anisotropy constrains net rotation of the lithosphere.  
769 *Geophys. Res. Lett.* 35, L05303. <https://doi.org/10.1029/2007GL032928>

770 Becker, T.W., Chevrot, S., Schulte-Pelkum, V., Blackman, D.K., 2006. Statistical properties  
771 of seismic anisotropy predicted by upper mantle geodynamic models. *Journal of*  
772 *Geophysical Research: Solid Earth* 111. <https://doi.org/10.1029/2005JB004095>

773 Becker, T.W., Conrad, C.P., Schaeffer, A.J., Lebedev, S., 2014. Origin of azimuthal seismic  
774 anisotropy in oceanic plates and mantle. *Earth and Planetary Science Letters* 401, 236–250.  
775 <https://doi.org/10.1016/j.epsl.2014.06.014>

776 Becker, T.W., Kawakatsu, H., 2011. On the role of anisotropic viscosity for plate-scale flow.  
777 *Geophysical Research Letters* 38, 1–5. <https://doi.org/10.1029/2011GL048584>

778 Becker, T.W., Kellogg, J.B., Ekström, G., O’Connell, R.J., 2003. Comparison of azimuthal  
779 seismic anisotropy from surface waves and finite strain from global mantle-circulation  
780 models. *Geophys J Int* 155, 696–714. <https://doi.org/10.1046/j.1365-246X.2003.02085.x>

781 Becker, T.W., Kustowski, B., Ekström, G., 2008. Radial seismic anisotropy as a constraint for  
782 upper mantle rheology. *Earth and Planetary Science Letters* 267, 213–227.  
783 <https://doi.org/10.1016/j.epsl.2007.11.038>

784 Beghein, C., Yuan, K., Schmerr, N., Xing, Z., 2014. Changes in Seismic Anisotropy Shed  
785 Light on the Nature of the Gutenberg Discontinuity. *Science* 343, 1237–1240.  
786 <https://doi.org/10.1126/science.1246724>

787 Behn, M.D., Conrad, C.P., Silver, P.G., 2004. Detection of upper mantle flow associated with  
788 the African Superplume. *Earth and Planetary Science Letters* 224, 259–274.  
789 <https://doi.org/10.1016/j.epsl.2004.05.026>

790 Bercovici, D., Ricard, Y., Richards, M.A., 2000. The Relation between mantle dynamics and  
791 plate tectonics: A Primer, in: Richards, M.A., Gordon, R.G., van der Hilst, R.D. (Eds.),  
792 *Geophysical Monograph Series*. American Geophysical Union, Washington, D. C., pp. 5–  
793 46. <https://doi.org/10.1029/GM121p0005>

794 Blackman, D.K., Boyce, D.E., Castelnau, O., Dawson, P.R., Laske, G., 2017. Effects of  
795 crystal preferred orientation on upper-mantle flow near plate boundaries: rheologic  
796 feedbacks and seismic anisotropy. *Geophysical Journal International* 210, 1481–1493.  
797 <https://doi.org/10.1093/gji/ggx251>

798 Boneh, Y., Morales, L.F.G., Kaminski, E., Skemer, P., 2015. Modeling olivine CPO evolution  
799 with complex deformation histories: Implications for the interpretation of seismic anisotropy  
800 in the mantle. *Geochemistry, Geophysics, Geosystems* 16, 3436–3455.  
801 <https://doi.org/10.1002/2015GC005964>

802 Bunge, H., 1982. *Texture Analysis in Materials Science: Mathematical Models*. Butterworths,  
803 London.

804 Capitanio, F.A., Faccenna, C., Zlotnik, S., Stegman, D.R., 2011. Subduction dynamics and  
805 the origin of Andean orogeny and the Bolivian orocline. *Nature* 480.

806 Christensen, N.I., 1984. The magnitude, symmetry and origin of upper mantle anisotropy  
807 based on fabric analyses of ultramafic tectonites. *Geophysical Journal International* 76, 89–  
808 111. <https://doi.org/10.1111/j.1365-246X.1984.tb05025.x>

809 Christensen, U.R., 1987. Some geodynamical effects of anisotropic viscosity. *Geophysical*  
810 *Journal of the Royal Astronomical Society* 91, 711–736. <https://doi.org/10.1111/j.1365-246X.1987.tb01666.x>

812 Conrad, C.P., Behn, M.D., 2010. Constraints on lithosphere net rotation and asthenospheric  
813 viscosity from global mantle flow models and seismic anisotropy: ANISOTROPY AND  
814 LITHOSPHERE NET ROTATION. *Geochem. Geophys. Geosyst.* 11, n/a-n/a.  
815 <https://doi.org/10.1029/2009GC002970>

816 Conrad, C.P., Lithgow-Bertelloni, C., 2004. The temporal evolution of plate driving forces:  
817 Importance of “slab suction” versus “slab pull” during the Cenozoic. *Journal of Geophysical*  
818 *Research B: Solid Earth* 109, 1–14. <https://doi.org/10.1029/2004JB002991>

819 Cramer, F., Magni, V., Domeier, M., Shephard, G.E., Chotalia, K., Cooper, G., Eakin, C.M.,  
820 Grima, A.G., Gürer, D., Király, Á., Mulyukova, E., Peters, K., Robert, B., Thielmann, M.,  
821 2020. A transdisciplinary and community-driven database to unravel subduction zone  
822 initiation. *Nature Communications* 11, 3750. <https://doi.org/10.1038/s41467-020-17522-9>

823 Dellinger, J., Vasicek, D., Sondergeld, C., 1998. Kelvin Notation for Stabilizing Elastic-  
824 Constant Inversion. *Revue de l'Institut Français du Pétrole* 53, 709–719.  
825 <https://doi.org/10.2516/ogst:1998063>

826 Durham, W.B., Goetze, C., 1977. Plastic flow of oriented single crystals of Olivine 1.  
827 Mechanical Data. *Journal of Geophysical Research* 82, 5737–5753.

828 Eakin, C.M., Rychert, C.A., Harmon, N., 2018. The Role of Oceanic Transform Faults in  
829 Seafloor Spreading: A Global Perspective From Seismic Anisotropy. *Journal of Geophysical*  
830 *Research: Solid Earth* 123, 1736–1751. <https://doi.org/10.1002/2017JB015176>

831 Faccenna, C., Becker, T.W., Lallemand, S., Steinberger, B., 2012. On the role of slab pull in  
832 the Cenozoic motion of the Pacific plate. *Geophysical Research Letters* 39, 1–6.  
833 <https://doi.org/10.1029/2011GL050155>

834 Gaboret, C., Forte, A.M., Montagner, J.-P., 2003. The unique dynamics of the Pacific  
835 Hemisphere mantle and its signature on seismic anisotropy. *Earth and Planetary Science*  
836 *Letters* 208, 219–233. [https://doi.org/10.1016/S0012-821X\(03\)00037-2](https://doi.org/10.1016/S0012-821X(03)00037-2)

837 Gerya, T.V., 2016. Origin, Evolution, Seismicity, and Models of Oceanic and Continental  
838 Transform Boundaries, in: *Plate Boundaries and Natural Hazards*. American Geophysical  
839 Union (AGU), pp. 39–76. <https://doi.org/10.1002/9781119054146.ch3>

840 Gurnis, M., Hall, C., Lavier, L., 2004. Evolving force balance during incipient subduction.  
841 *Geochemistry, Geophysics, Geosystems* 5. <https://doi.org/10.1029/2003GC000681>

842 Hansen, L.N., Conrad, C.P., Boneh, Y., Skemer, P., Warren, J.M., Kohlstedt, D.L., 2016a.  
843 Viscous anisotropy of textured olivine aggregates: 2. Micromechanical model. *Journal of*  
844 *Geophysical Research: Solid Earth* 121, 7137–7160. <https://doi.org/10.1002/2016JB013304>

845 Hansen, L.N., Warren, J.M., Zimmerman, M.E., Kohlstedt, D.L., 2016b. Viscous anisotropy  
846 of textured olivine aggregates, Part 1: Measurement of the magnitude and evolution of  
847 anisotropy. *Earth and Planetary Science Letters* 445, 92–103.  
848 <https://doi.org/10.1016/j.epsl.2016.04.008>

849 Hansen, L.N., Zimmerman, M.E., Kohlstedt, D.L., 2012. Laboratory measurements of the  
850 viscous anisotropy of olivine aggregates. *Nature* 492, 415–418.  
851 <https://doi.org/10.1038/nature11671>

852 Jahren, A.H., Conrad, C.P., Arens, N.C., Mora, G., Lithgow-Bertelloni, C., 2005. A plate  
853 tectonic mechanism for methane hydrate release along subduction zones. *Earth and Planetary*  
854 *Science Letters* 236, 691–704. <https://doi.org/10.1016/j.epsl.2005.06.009>

855 Kaminski, É., Ribe, N.M., 2002. Timescales for the evolution of seismic anisotropy in mantle  
856 flow. *Geochemistry, Geophysics, Geosystems* 3, 1–17.  
857 <https://doi.org/10.1029/2001GC000222>

858 Karato, S., 1987. Seismic anisotropy due to lattice preferred orientation of minerals:  
859 Kinematic or dynamic?, in: Manghnani, M.H., Syono, Y. (Eds.), *Geophysical Monograph*  
860 *Series*. American Geophysical Union, Washington, D. C., pp. 455–471.  
861 <https://doi.org/10.1029/GM039p0455>

862 Karato, S., Wu, P., 1993. Rheology of the Upper Mantle: A Synthesis. *Science* 260, 771–778.

863 Lev, E., Hager, B.H., 2011. Anisotropic viscosity changes subduction zone thermal structure.  
864 *Geochemistry, Geophysics, Geosystems* 12. <https://doi.org/10.1029/2010GC003382>

865 Lev, E., Hager, B.H., 2008. Rayleigh-Taylor instabilities with anisotropic lithospheric  
866 viscosity. *Geophysical Journal International* 173, 806–814. <https://doi.org/10.1111/j.1365->  
867 [246X.2008.03731.x](https://doi.org/10.1111/j.1365-246X.2008.03731.x)

868 Long, M.D., 2013. Constraints on Subduction Geodynamics From Seismic Anisotropy.  
869 *Reviews of Geophysics* 51, 76–112. <https://doi.org/10.1002/rog.20008>

870 Long, M.D., Becker, T.W., 2010. Mantle dynamics and seismic anisotropy. *Earth and*  
871 *Planetary Science Letters* 297, 341–354. <https://doi.org/10.1016/j.epsl.2010.06.036>

872 Mainprice, D., Bachmann, F., Hielscher, R., Schaeben, H., 2015. Descriptive tools for the  
873 analysis of texture projects with large datasets using MTEX: strength, symmetry and  
874 components. *Geological Society, London, Special Publications* 409, 251–271.  
875 <https://doi.org/10.1144/SP409.8>

876 Mühlhaus, H.-B., Čada, M., Moresi, L., 2003. Anisotropic Convection Model for the Earth's  
877 Mantle, in: Sloot, P.M.A., Abramson, D., Bogdanov, A.V., Gorbachev, Y.E., Dongarra, J.J.,  
878 Zomaya, A.Y. (Eds.), *Computational Science — ICCS 2003*. Springer Berlin Heidelberg,  
879 Berlin, Heidelberg, pp. 788–797. [https://doi.org/10.1007/3-540-44863-2\\_77](https://doi.org/10.1007/3-540-44863-2_77)

880 Mühlhaus, H.-B., Moresi, L., Hobbs, B., Dufour, F., 2002. Large Amplitude Folding in Finely  
881 Layered Viscoelastic Rock Structures. *Pure and Applied Geophysics* 159, 2311–2333.  
882 <https://doi.org/10.1007/s00024-002-8737-4>

883 Pouilloux, L., Kaminski, E., Labrosse, S., 2007. Anisotropic rheology of a cubic medium and  
884 implications for geological materials. *Geophysical Journal International* 170, 876–885.  
885 <https://doi.org/10.1111/j.1365-246X.2007.03461.x>

886 Richards, M.A., Lithgow-Bertelloni, C., 1996. Plate motion changes, the Hawaiian-Emperor  
887 bend, and the apparent success and failure of geodynamic models. *Earth and Planetary  
888 Science Letters* 137, 19–27. [https://doi.org/10.1016/0012-821X\(95\)00209-U](https://doi.org/10.1016/0012-821X(95)00209-U)

889 Schellart, W.P., 2004. Kinematics of subduction and subduction-induced flow in the upper  
890 mantle. *Journal of Geophysical Research B: Solid Earth* 109, 1–19.  
891 <https://doi.org/10.1029/2004JB002970>

892 Signorelli, J., Tommasi, A., 2015. Modeling the effect of subgrain rotation recrystallization  
893 on the evolution of olivine crystal preferred orientations in simple shear. *Earth and Planetary  
894 Science Letters* 430, 356–366. <https://doi.org/10.1016/j.epsl.2015.08.018>

895 Silver, P.G., 1996. SEISMIC ANISOTROPY BENEATH THE CONTINENTS: Probing the  
896 Depths of Geology. *Annu. Rev. Earth Planet. Sci.* 24, 385–432.  
897 <https://doi.org/10.1146/annurev.earth.24.1.385>

898 Skemer, P., Katayama, I., Jiang, Z., Karato, S., 2005. The misorientation index: Development  
899 of a new method for calculating the strength of lattice-preferred orientation. *Tectonophysics*  
900 411, 157–167. <https://doi.org/10.1016/j.tecto.2005.08.023>

901 Stixrude, L., Lithgow-Bertelloni, C., 2005. Mineralogy and elasticity of the oceanic upper  
902 mantle: Origin of the low-velocity zone. *Journal of Geophysical Research: Solid Earth* (1978–  
903 2012) 110. <https://doi.org/10.1029/2004JB002965>

904 Tanimoto, T., Anderson, D.L., 1984. Mapping convection in the mantle. *Geophysical  
905 Research Letters* 11, 287–290. <https://doi.org/10.1029/GL011i004p00287>

906 Taylor, G.I., 1938. Plastic Strain in Metals. *Journal of Inst. Met.* 62.

907 Tommasi, A., 1998. Forward modeling of the development of seismic anisotropy in the upper  
908 mantle. *Earth and Planetary Science Letters* 160, 1–13. [https://doi.org/10.1016/S0012-  
909 821X\(98\)00081-8](https://doi.org/10.1016/S0012-821X(98)00081-8)

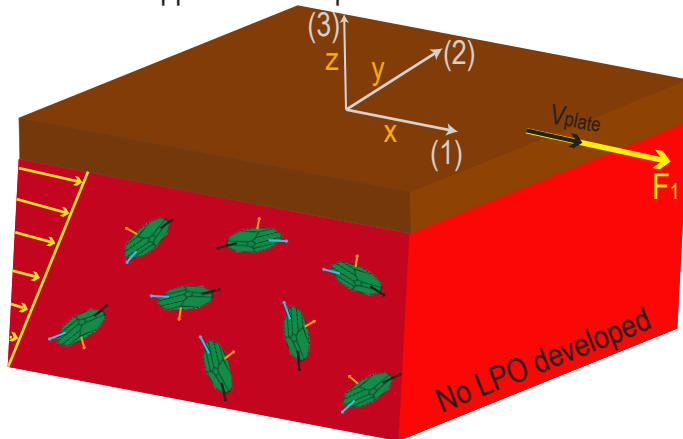
910 Vollmer, F.W., 1990. An application of eigenvalue methods to structural domain analysis.  
911 *Bulletin of the Geological Society of America* 102, 786–791. [https://doi.org/10.1130/0016-  
912 7606\(1990\)102<0786:AAOEMT>2.3.CO;2](https://doi.org/10.1130/0016-7606(1990)102<0786:AAOEMT>2.3.CO;2)

913 Yuan, H., Romanowicz, B., 2010. Lithospheric layering in the North American craton. *Nature*  
914 466, 1063–1068. <https://doi.org/10.1038/nature09332>

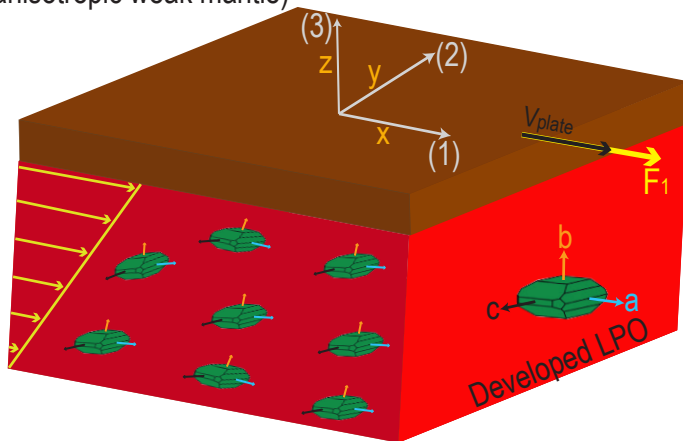
915

916 **Figures**

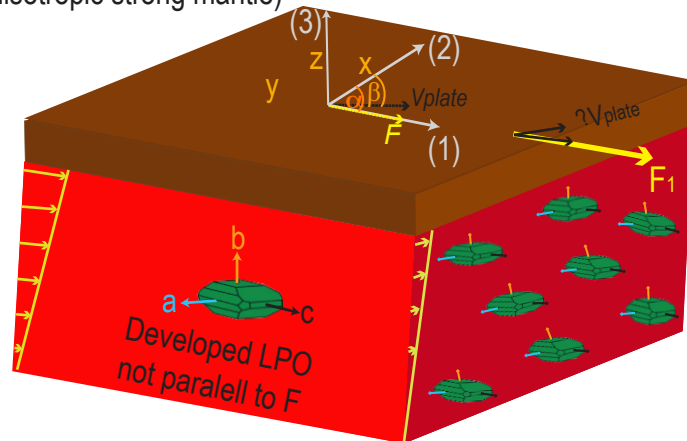
A) Shear force applied to isotropic mantle



B) Shear force applied parallel to developed LPO (anisotropic weak mantle)



C) Shear force applied perpendicular to LPO (anisotropic strong mantle)

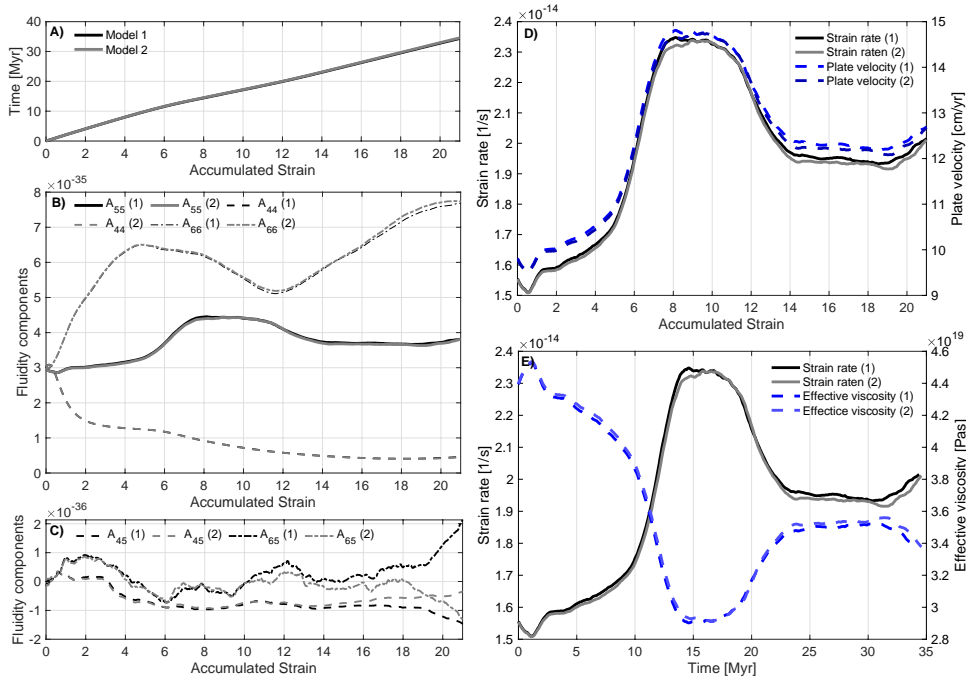


917

918 *Figure 1: Relationship between anisotropic viscosity and olivine texture formation. A) A force*  
 919 *( $F_1$ ) applied to an initially isotropic asthenosphere (i.e., without a pre-existing texture) yields*  
 920 *a moderate plate speed, and the associated asthenospheric deformation fosters olivine texture*  
 921 *development. B) The same force applied parallel to the a-axis of a well-developed texture*  
 922 *results in a much larger plate speed. C) Applying this force parallel to the c-axis causes the*

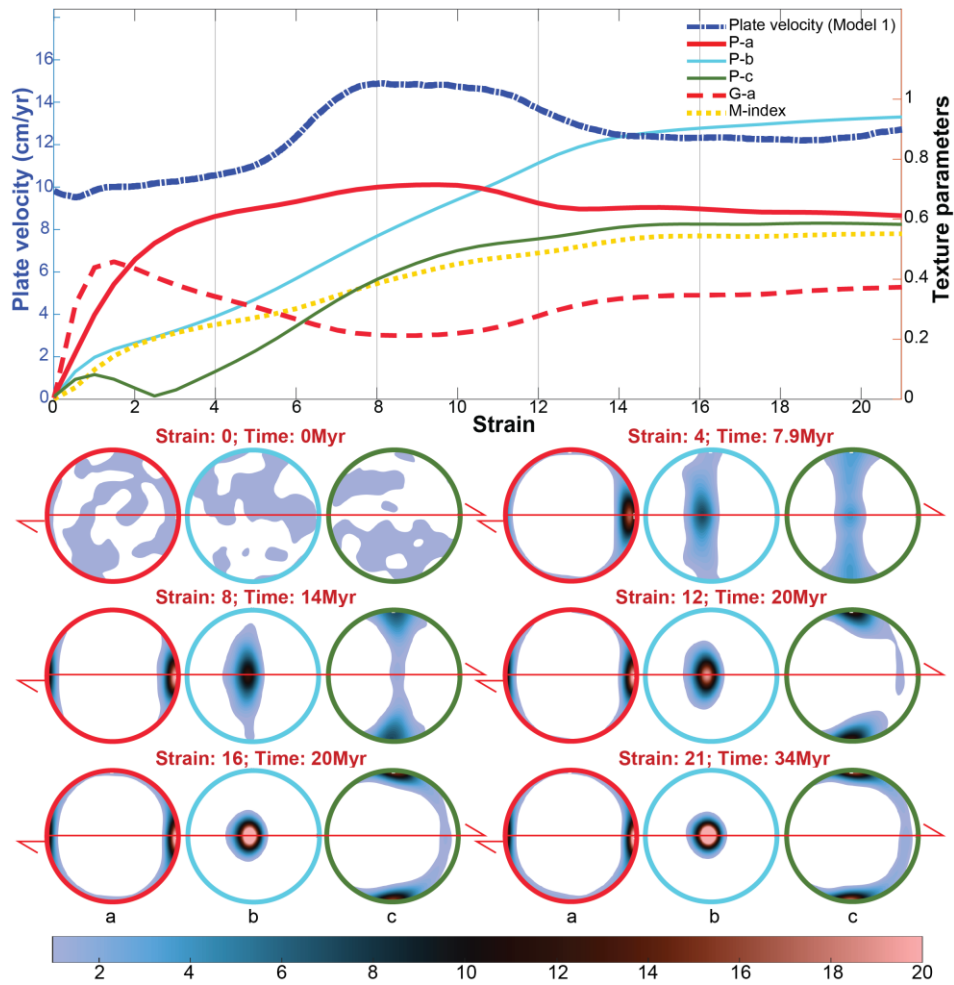
923 plate to move much more slowly. The configuration depicted in panel (B) can evolve into the  
 924 configuration depicted in panel (C) in two ways. Either the force can be rotated relative to the  
 925 texture (as for many geodynamic scenarios) or the texture can be rotated with respect to the  
 926 force (as illustrated in (C) and implemented in our modeling effort).

927



928

929 *Figure 2: Results of two sets of models with constant shear stress ( $\sigma_{13} = 0.68$  MPa), both*  
 930 *computed as average results from 5 model runs each starting from 1000 uniformly distributed*  
 931 *grain orientations. A) Accumulated strain as a function of time. B) Shear components of the*  
 932 *fluidity parameter tensor.  $A_{44}$  and  $A_{66}$  are fictive curves since the associated stresses for these*  
 933 *components,  $\sigma_{23}$  and  $\sigma_{12}$ , are zero.  $A_{55}$  represents the fluidity for the actual applied stress  $\sigma_{13}$ .*  
 934 *C) Fluidity components relating strain rates in the perpendicular direction ( $A_{45}$ ) or plane*  
 935 *( $A_{65}$ ) with respect to the shear stress ( $\sigma_{13}$ ). D) Strain rate ( $|\dot{\epsilon}|$ ) and plate velocity ( $v_{\text{plate}}$ ) as a*  
 936 *function of the accumulated strain. The plate velocity is calculated from the horizontal strain*  
 937 *rate component (eq. 10), while the strain-rate curve is the norm of the shear strain rate tensor*  
 938 *(for which only the non-diagonal components are non-zero). E) Strain rate and effective*  
 939 *viscosity as a function of time instead of accumulated strain.*

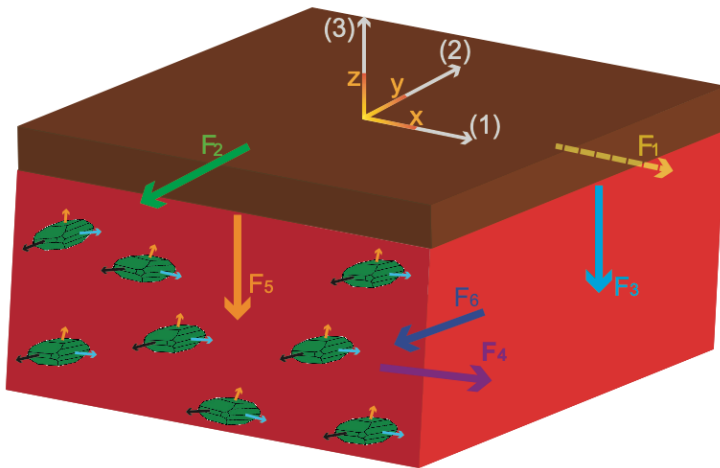


940

941 *Figure 3: The evolution of plate velocity and several texture parameters as a function of*  
 942 *accumulated strain (top panel) with pole figures (below) indicating the orientation density of*  
 943 *a-, b-, and c- axes for olivine aggregates with different total strains. The color scale indicates*  
 944 *multiples of a uniform density. The shear direction (marked by red arrows) is towards the*  
 945 *right and the shear plane is the same as the figure's plane.*

946

## Possibilities for changing the shear force

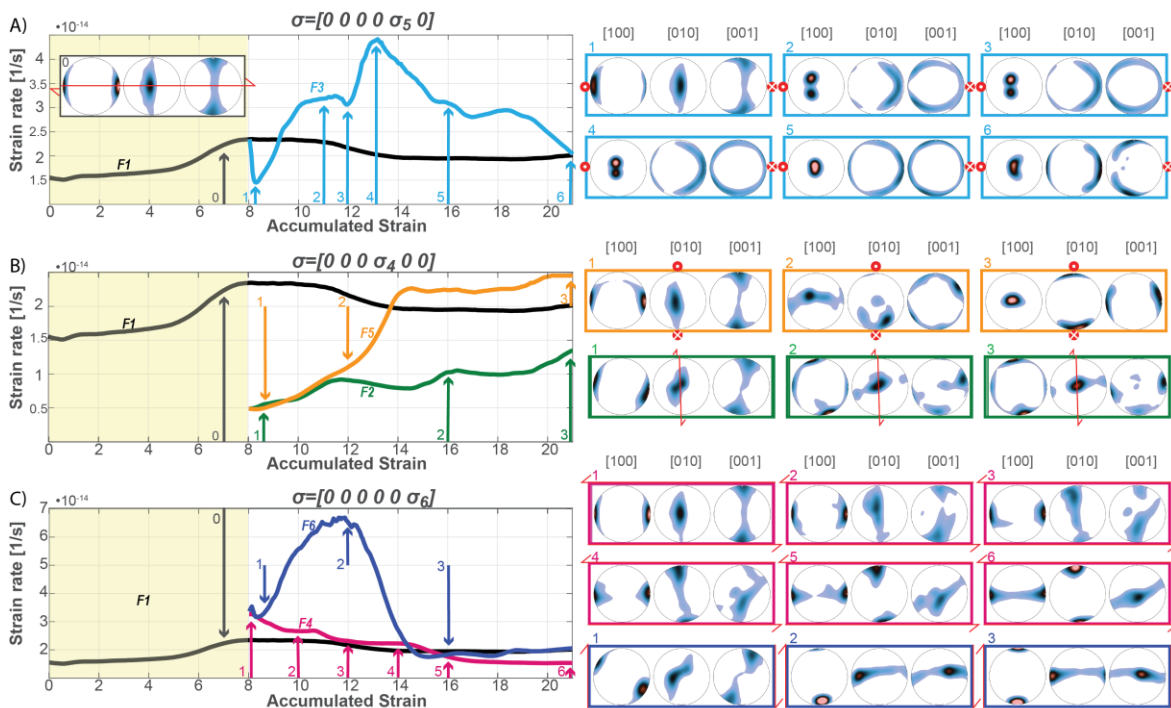


947

948 *Figure 4: Possible orientations for the shear force, with  $F_1$  representing the orientation*  
 949 *associated with initial plate motion (e.g., as in Fig. 1b).  $F_2$  represents a shear force acting on*  
 950 *a horizontal plane at  $90^\circ$  to the initial plate motion direction, analogous to a change in the*  
 951 *direction of the plate driving force.  $F_4$  and  $F_6$  represent forces that create shearing*  
 952 *deformation in a horizontal direction along vertical planes, analogous to transform shear*  
 953 *zones.  $F_3$  and  $F_5$  represent forces that create shearing deformation in a vertical direction on*  
 954 *vertical planes, analogous to subduction initiation or a dripping instability. In our analysis,*  
 955 *all forces have the same magnitude as  $F_1$ .*

956

957

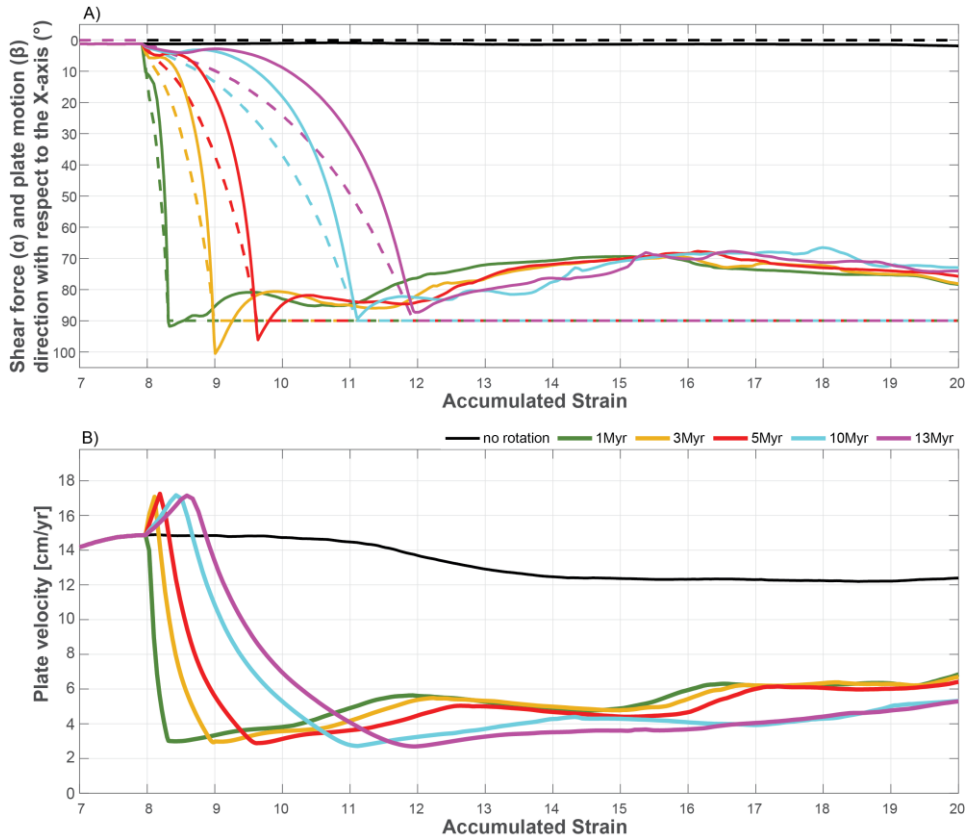


958

959 *Figure 5: Strain rate as a function of accumulated strain for the five different changes to the*  
 960 *imposed shear force (Fig. 4). On the left side, an initially isotropic aggregate is deformed*

961 with shear force  $F_1$  until a strain of 8 (as in Fig. 2D). At a strain of 8, the direction of the  
 962 shear force is instantaneously changed to the directions  $F_2$  through  $F_6$  (Fig. 4). Plots are  
 963 grouped based on reciprocal pairs of deformation responding to the same imposed stress (see  
 964 text). On the right side, pole figures indicate the texture for several points in the evolution  
 965 denoted by arrows in the left diagrams. Note that all of the textures are presented relative to  
 966 the mantle reference frame, and the shear force acting on the mantle is marked by red arrows  
 967 (and arrow points and tails).

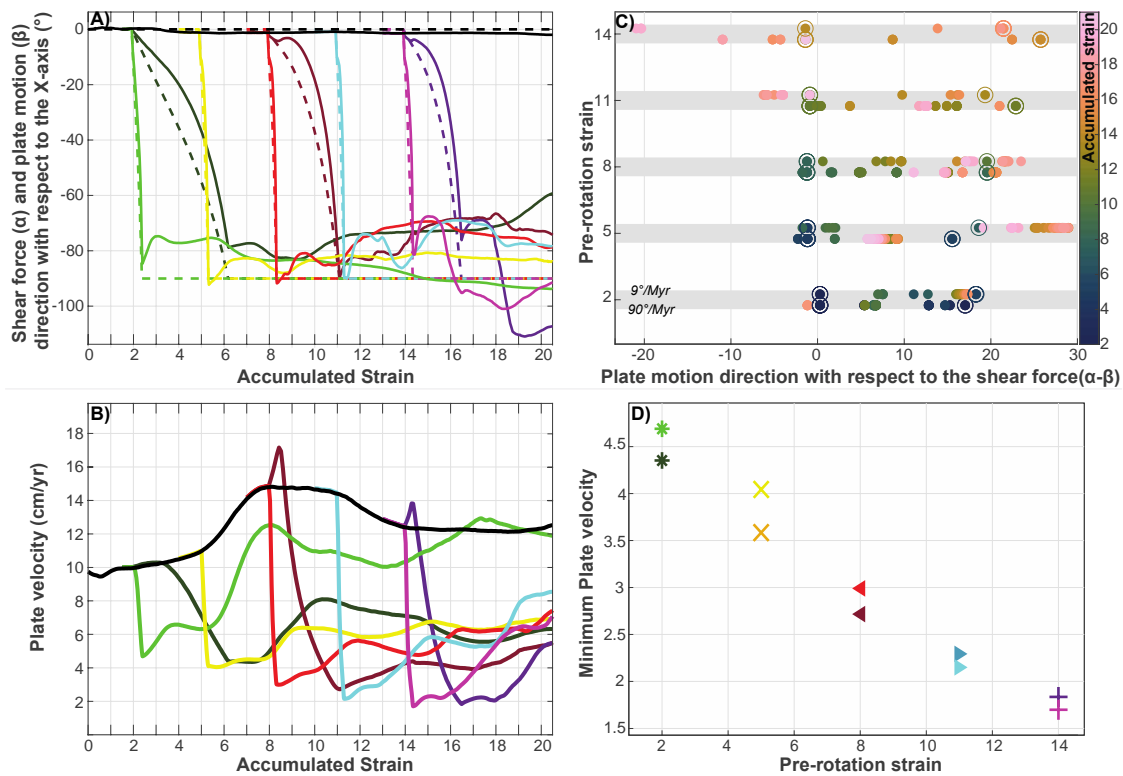
968



969

970 *Figure 6: Results from models with different rates of imposed rotation of the shear stress. An*  
 971 *initial texture (associated with an accumulated strain of 8, using model 1 of Fig. 2) is rotated*  
 972 *90° around the z-axis (representing a change from  $F_1$  to  $F_2$ ) within a period between 1 and 13*  
 973 *Myr. a) Change in the direction of the shear force ( $\alpha$ , dashed lines) and plate motion ( $\beta$ , solid*  
 974 *lines) with respect to the x-axis (fixed to the mantle), as a function of accumulated strain. b)*  
 975 *Amplitude of the plate velocity as a function of accumulated strain.*

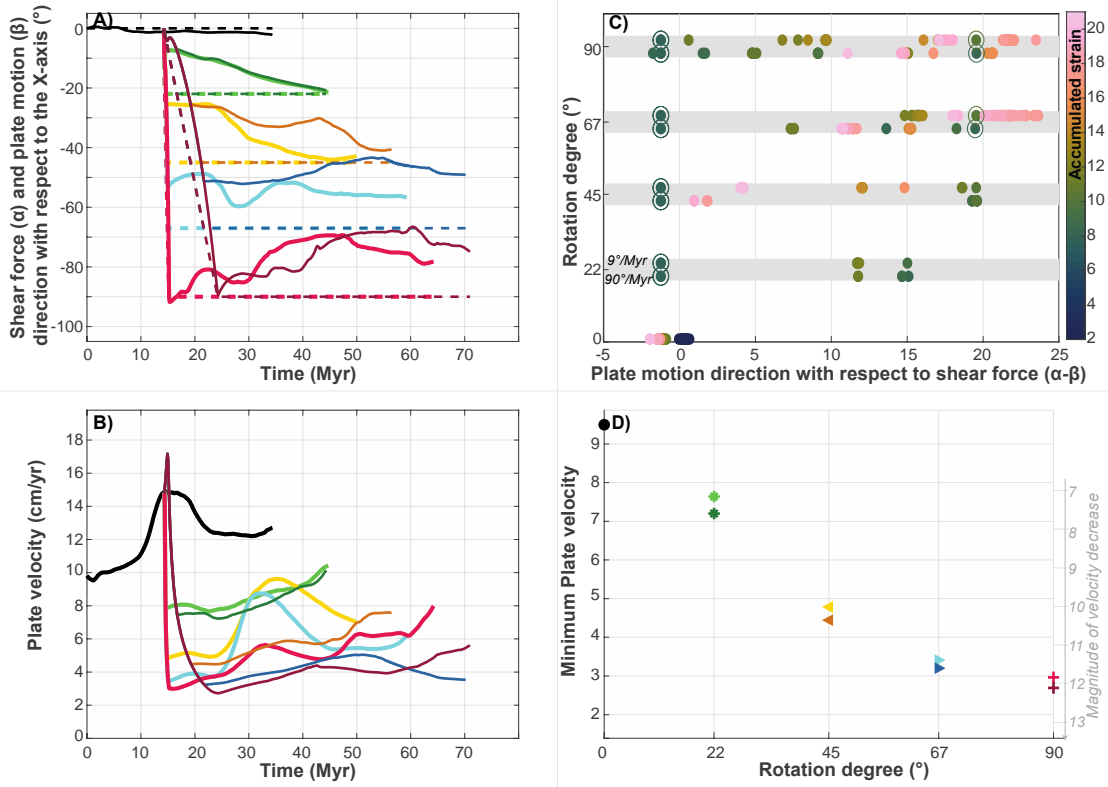
976



977

978 *Figure 7: Results from models with varying amounts of accumulated strain (and therefore*  
 979 *texture strength) at the time of the rotation (Pre-rotation strain). A) Direction of the shear*  
 980 *force ( $\alpha$ , dashed lines) and the plate motion ( $\beta$ , solid lines) for models that rotate the texture*  
 981 *90° in either 1 Myr (lighter colors) or 10 Myr (darker colors). B) Corresponding plate*  
 982 *velocity amplitudes vs. accumulated strain for the cases shown in (A). C) Local minimums*  
 983 *and maximums of the plate-motion direction marked with dots that are color-coded according*  
 984 *the accumulated strain (with respect to the shear force direction) for the five tested pre-*  
 985 *rotation strains. For each switch strain, upper rows represent models using the 10 Myr*  
 986 *rotation time while the lower rows use 1 Myr rotations. D) Minimum plate velocity (i.e.,*  
 987 *velocity right after the rotation) vs. the accumulated strain after which the rotation has*  
 988 *happened.*

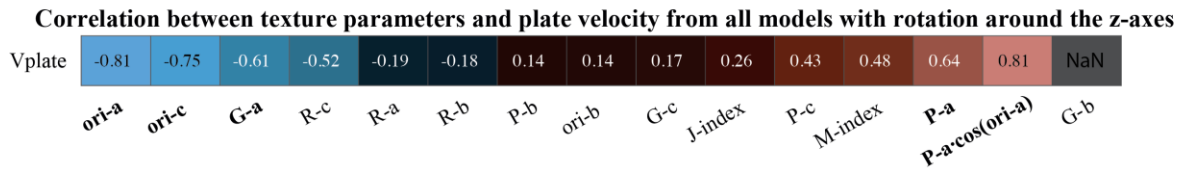
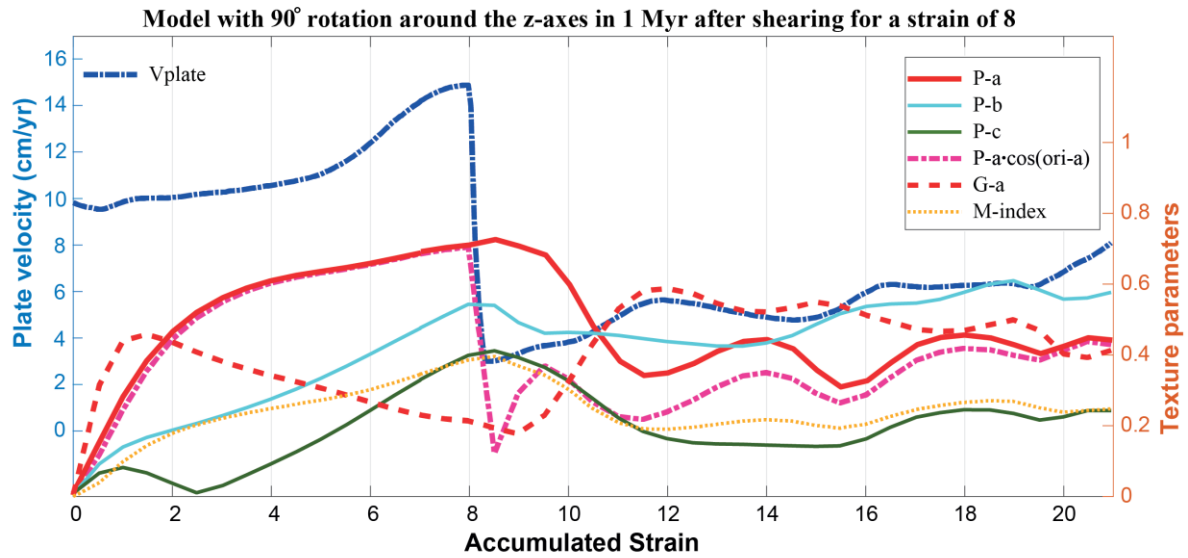
989



990

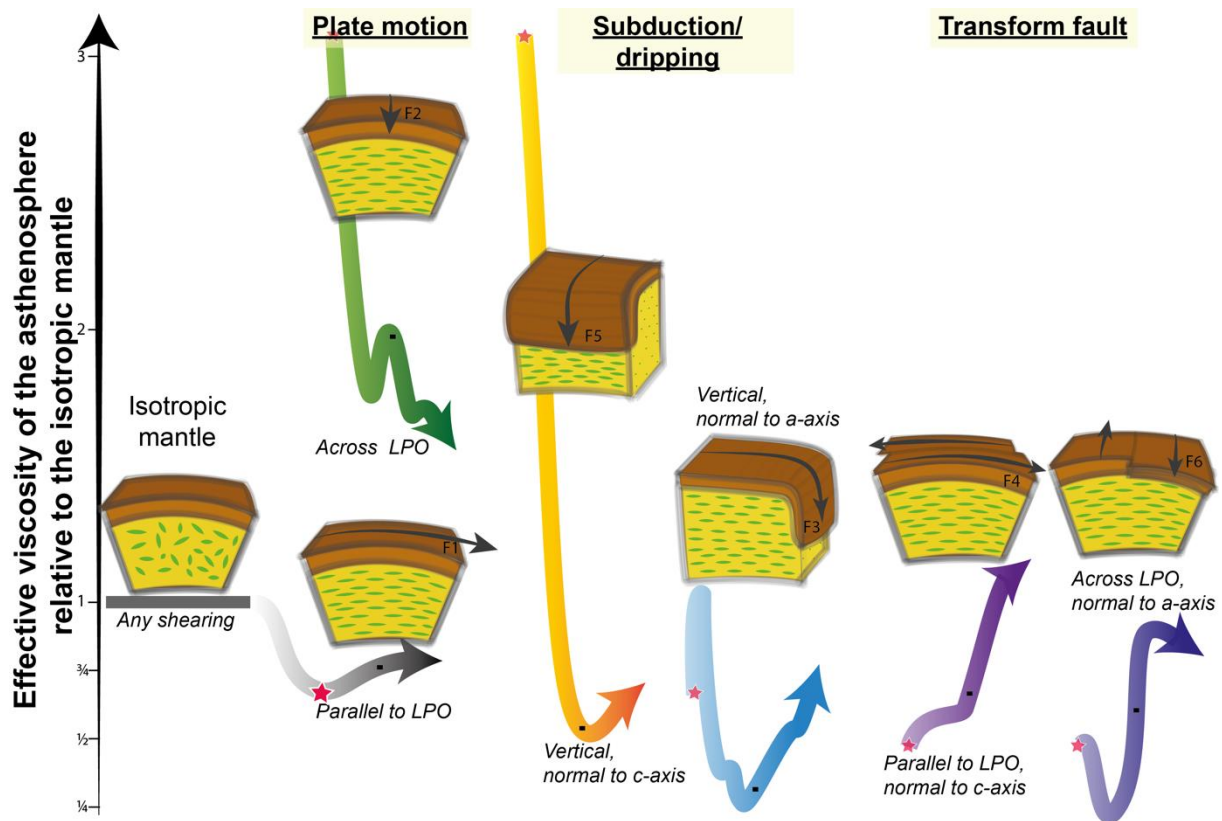
991 *Figure 8: Results from models with varying amounts of rotation around the z-axis. Panels are*  
 992 *the same as in Fig. 7, except using rotation angle instead of pre-rotation strain in (C) and*  
 993 *(D).*

994



995

996 *Figure 9: Top) plate velocity and texture parameters, as a function of accumulated strain, for*  
 997 *a model in which a 90° rotation (representing a change from  $F_1$  to  $F_2$ ) is imposed over 1 Myr*  
 998 *after a strain of 8 (the fastest rotation presented in Fig. 6). Bottom) correlation between*  
 999 *texture parameters and plate velocity based on all models with rotation (0-90°) around the z-*  
 1000 *axis, listed in order from negative (blue shades) to positive (red shades) correlations.*  
 1001 *Abbreviations:  $v_{plate}$  plate velocity; ori-a (-b; -c) mean orientation of the olivine a-axes (b-*  
 1002 *axes; c-axes); G, R, P (-a -b; -c) girdle, random, and point distribution parameters for each*  
 1003 *axes, respectively (Vollmer, 1990).*



1004

1005 *Figure 10: Trends for the manner in which anisotropic viscosity in the asthenosphere should*  
 1006 *influence different geodynamic situations. The white to black arrow indicates the mantle*  
 1007 *weakening path associated with development of an LPO as the asthenosphere accumulates*  
 1008 *strain due to simple shear (e.g. in model 1). The colored arrows indicate the time evolution of*  
 1009 *the relative effective viscosity (vertical dimension, values based on results shown in Fig. 5)*  
 1010 *from the moment of switching the shear direction (strain of 8, marked with a star) through an*  
 1011 *accumulated strain of 14 (post-rotation strain of 6, black squares), and until a strain of 21*  
 1012 *(post-rotation strain of 13, indicated by the arrow tips). Geodynamic processes for which the*  
 1013 *effective viscosity increases (F<sub>2</sub> plate motion and F<sub>5</sub> subduction/dripping) could be initially*  
 1014 *impeded by anisotropic viscosity, while those for which the effective viscosity decreases (F<sub>3</sub> -*  
 1015 *subduction and dripping, and F<sub>4</sub> and F<sub>5</sub> - transform fault) could be initially promoted.*  
 1016 *Subsequent changes to the effective viscosity along each path indicate how continued texture*  
 1017 *development should either speed or slow each process as it develops.*